Submitted to *Int. J. Mass Spectrom.*

Thermochemical Studies of Hydrated Manganese Dications, $Mn^{2+}(H_2O)_x$ (x = 4 – 9), Using Guided Ion Beam Tandem Mass Spectrometry

Fan Yang, Rebecca Coates, Georgia C. Boles, and P. B. Armentrout*

Department of Chemistry, University of Utah, 315 S. 1400 E. Rm 2020, Salt Lake City, UT 84112

ABSTRACT

The experimental hydration energies of $Mn^{2+}(H_2O)_x$ complexes, where x = 4 - 9, are determined by threshold collision-induced dissociation (TCID) with Xe using a guided ion beam tandem mass spectrometer, coupled with an electrospray ionization (ESI) source. The ESI source naturally produces intense beams of the x = 7 – 9 complexes, but smaller complexes, x = 4 – 6, can be formed using an in-source fragmentation technique. For all systems, the dominant fragmentation processes observed are sequential loss of water ligands, but at x = 4 and 5, charge separation (CS) reactions are observed where formation of singularly charged species becomes competitive. Kinetic energy-dependent cross sections are obtained and analyzed to yield 0 K bond dissociation energies (BDEs) for the losses of one and two water ligands, which are then converted to 298 K binding enthalpies and Gibbs energies. Barrier heights for three different CS reactions are also determined. These thermodynamic results are compared with values obtained theoretically, with reasonable agreement being achieved. Theoretical geometry and single-point energy calculations are performed at B3LYP, B3P86, M06, and MP2(full) levels of theory.

INTRODUCTION

Manganese (Mn) is a 3d transition metal that occurs naturally and exists in a variety of forms. Like other metals, Mn is essential for many biological processes but can be toxic in high concentration with excess intake causing neurological damage [1]. Mn is generally obtained through inhalation or ingestion. Because waterborne Mn has higher bioavailability than dietary Mn, drinking water becomes the most likely source of Mn toxicity [2]. As such, extensive research has been conducted to investigate the metal ion interactions with aqueous media in order to understand the fundamentals of these intermolecular interactions.

Paul Kebarle was a pioneer in the study of the thermochemistry of metal-water complexes, using ion equilibria to measure a host of hydrated metal ion complexes [3-9]. Since his early work, additional mass spectrometry techniques have been used, such as blackbody infrared radiative dissociation (BIRD) [10, 11] and collision-induced dissociation (CID) by Kebarle [12-14] and others [15]. In the present work, thermochemical information regarding $Mn^{2+}(H_2O)_x$, where $x = 3 – 9$, is determined using threshold collision-induced dissociation (TCID) and complemented with theoretical calculations. This extends work conducted over the past several years in which the Armentrout group has studied the thermochemistry of the hydration of groups 2 and 12 [16-23] and late 3d transition metal dications, $M^{2+}(H_2O)_x$ where M = Fe [24], Co [25], Ni [26], Cu [27], Zn [18, 19] and $MOH^+(H_2O)_x$ where M = Fe [28], Co [29], and Cu [30] in the gas-phase. In all cases, TCID was carried out in a guided ion beam tandem mass spectrometer (GIBMS) to accurately and directly measure the hydration energies of the metal ion-water complexes. In agreement with previous TCID studies of $M^{2+}(H_2O)_x$, the dominant process observed in the present study of $Mn^{2+}(H_2O)_x$ is loss of a single water ligand as shown in reaction (1),

$$Mn^{2+}(H_2O)_x \rightarrow Mn^{2+}(H_2O)_{x-1} + H_2O \quad (1)$$

followed by sequential loss of additional water molecules. In addition, at particular sizes of $Mn^{2+}(H_2O)_x$, the doubly charged complexes dissociate into two singly charged species in a process competitive with the loss of water. This charge separation (CS) reaction is shown in reaction (2).

$$Mn^{2+}(H_2O)_x \rightarrow MnOH^+(H_2O)_y + H^+(H_2O)_{x-y-1} \quad (2)$$

The phenomenon of reaction (2) for hydrated transition metal dications has been studied to determine the critical size, x_{crit}, which has been defined as "the maximum number of ligands at which dissociative charge transfer is competitive with simple ligand loss" [15]. For manganese, Kebarle and co-workers reported that the largest complex size for which CS occurred was $x_{crit} = 3$ [5, 6, 12], whereas Shvartzburg and Siu suggested $x_{crit} = 4$ [15]. Such dichotomies have led to a more precise redefinition of the critical size as "the largest value of x at which the charge separation is energetically favored over the loss of one water ligand" [18]. Previous TCID studies from the Armentrout group have determined the energy-dependent x_{crit} for late 3d transition metals: 4 for Fe^{2+} [24], 6 for Co^{2+} [25], 4 for Ni^{2+} [26], 8 for Cu^{2+} [27], and 7 for Zn^{2+} [19].

In addition to the experimental work, the present study includes theory to determine the rate-limiting steps for the observed reactions, which gives an in-depth analysis of how the competitive water loss and charge separation reactions proceed. Theory also provides the structures of the complexes, thereby allowing evaluation of the coordination number of the metal center. The present work reports the experimental energies required to lose a water molecule from $Mn^{2+}(H_2O)_x$, where $x = 4 – 9$, and the barriers to several CS processes. Theoretical values reproduce these experimental findings and together yield fundamental information regarding how Mn^{2+} interacts with water.

EXPERIMENTAL AND COMPUTATIONAL METHODS

Experimental Procedures. TCID cross sections of $Mn^{2+}(H_2O)_x$ with xenon (Xe) were measured directly using a GIBMS, which has been described in detail elsewhere [31, 32]. The hydrated manganese dications, $Mn^{2+}(H_2O)_x$, were generated from a 10^{-4} M solution of $MnCl_2$ in HPLC grade water using an electrospray ionization (ESI) source [33]. The solution was pumped through an electrospray needle at a low flow rate of 0.08 – 0.10 L/hr with an applied voltage of negative 2.0 – 2.2 kV. The ions were introduced into the vacuum system through an inlet cap

followed by a heated capillary (80 °C) to promote desolvation of large droplets. As the ions exited the capillary, they were collected by an 88-plate radio-frequency (rf) ion funnel [34], which pulled the ions through using a DC-gradient, typically 2 - 5 V. At the end of the funnel, ions were injected into a rf-only hexapole ion guide, where the ions were trapped radially with an rf amplitude of 250 V peak-to-peak. For larger $Mn^{2+}(H_2O)_x$ complexes, $x = 7 – 9$, the ESI source generated sufficient intensity of the ions of interest; however, for smaller complexes, $x \leq 6$, an in-source fragmentation technique was needed. Here, negatively biased DC electrodes were placed in between the hexapole rods. The electrodes are believed to pull the ions towards the rods where collisional rf heating of the complexes can occur, with details described elsewhere [23, 35]. The technique was used to increase the intensity of the desired ions by fragmenting larger complexes. This enabled formation of complexes down to the $x = 4$ complex, where the charge separation reaction becomes more favorable than water loss (see below), such that smaller $Mn^{2+}(H_2O)_x$ complexes ($x < 4$) cannot be formed. Similar limitations have also been seen previously for hydrated cobalt [25], nickel [26], copper [27], and zinc dications [18]. After fragmentation, the ions underwent ~10^5 collisions with ambient gas as they drifted through the hexapole ion guide. As shown in previous studies, under proper conditions, the ions emerging from the hexapole are thermalized to room temperature (300 K) [17, 20, 23, 25, 26, 29, 35-37]. To further investigate the thermalization of the ions in this study, a cooling gas cell was placed around the hexapole. A low pressure (~2 mTorr) of nitrogen gas was introduced into the cell to enhance the thermalization conditions, although no changes in the TCID cross sections of the complexes were observed.

The ions were extracted from the hexapole ion guide and then focused into a magnetic momentum analyzer, where the desired complex was mass selected. These ions were decelerated to a well-defined kinetic energy and injected into a dual rf octopole ion guide where the ions were trapped radially [31, 32, 38]. In the middle of the first octopole, the ions passed through a collision cell containing low pressures (~0.05, 0.1, and 0.2 mTorr) of xenon (Xe) [39-41]. The unreacted precursor and collisionally formed product ions drifted to the end of the octopole where they were extracted, mass selected using a quadrupole mass filter, and detected using a Daly detector [42].

Data Analysis. Conversion of ion intensities into absolute cross sections has been described previously and uses a Beer-Lambert law analogue [31]. The cross sections have absolute uncertainties estimated at ±20% (10% uncertainties each in pressure measurement and collision cell length). The ions were accelerated in the octopole region by the laboratory voltage (V_{Lab}), which corresponds to half the ion kinetic energy for these doubly charged complexes. This voltage was converted to the relative kinetic energy in the center-of-mass (CM) frame, the maximum energy available to induce dissociation. The formula used was $E_{CM} = E_{Lab} \times m/(m + M)$, where $E_{Lab} = 2V_{Lab}$, m is the mass of the neutral collision gas (Xe), and M is the mass of the reactant ion. A retarding potential on the octopole was used to determine the absolute zero of energy and the kinetic energy distribution of the ion beam by taking the derivative of the normalized ion intensity versus kinetic energy and fitting to a Gaussian distribution (0.10 – 0.15 eV FWHM) [31]. All energies below are reported in the CM frame.

In order to extract accurate thermochemical information from the kinetic energy dependent cross sections, several factors have to be taken into consideration: multiple precursor-neutral collisions, lifetime effects, and additional energy distributions. Thus, the TCID experiments were performed at various pressures of Xe [43, 44], and the resulting cross sections were extrapolated to zero-pressure to ensure rigorous single-collision conditions. The zero-pressure extrapolated cross sections for loss of a single ligand were modeled using the empirical threshold model shown in Eq. (3):

$$\sigma_j(E) = \sigma_{0,j} \sum g_i \left(E + E_i - E_{0,j}\right)^n / E \qquad (3)$$

where $\sigma_{0,j}$ is an energy-independent scaling factor for product channel j, E is the relative translational energy of the reactants (E_{CM}), $E_{0,j}$ is the reaction threshold for channel j at 0 K, and n is an adjustable fitting parameter that describes the efficiency of the energy transfer upon collision [32]. The summation is over the ro-vibrational states of the reactants with excitation energies E_i and populations g_i, where $\Sigma g_i = 1$. The number of ro-vibrational states was directly counted by the Beyer-Swinehart-Stein-Rabinovich algorithm to evaluate the internal energy distribution for the reactants [45-47]. A Maxwell-Boltzmann distribution at 300 K was used to compute the relative

populations, g_i. Regarding lifetime effects, as the ions become larger and more complex, those with energy in excess of the dissociation energy may not have enough time to dissociate on the time scale of the experiment, $\tau \approx 5 \times 10^{-4}$ s [32]. This can result in a kinetic shift (or a delayed onset) in the apparent threshold for CID. To account for this effect, Rice−Ramsperger−Kassel−Marcus (RRKM) statistical theory [48-50] for unimolecular dissociation is incorporated into the empirical threshold model, as shown in Eq. (4) [51]:

$$\sigma_j(E) = \left(\frac{n\sigma_{0,j}}{E}\right) \sum g_i \int_{E_{0,j}-E_i}^{E} \left[\frac{k_j(E^*)}{k_{tot}(E^*)}\right] (E-\varepsilon)^{n-1}\ P_{D1} d(\varepsilon) \quad (4)$$

In Eq. (4), ε is the energy transferred into internal degrees of freedom of the reactant ion during collision, such that the energized molecule (EM) has an internal energy of $E^* = \varepsilon + E_i$, and $k_{tot}(E^*)$ is the total unimolecular dissociation rate constant. The rate constant was used to calculate a probability of dissociation, $P_{D1} = 1 - \exp\left[-k_{tot}(E^*)\tau\right]$, and is defined in Eq. (5),

$$k_{tot}(E^*) = \sum_j k_j(E^*) = \sum_j s_j N_j^{\dagger}\,(E^* - E_{0,j})/h\rho(E^*) \quad (5)$$

where $k_j(E^*)$ is the rate constant for a single dissociation channel j, s_j is the reaction degeneracy calculated from the ratio of rotational symmetry numbers of the reactants and products of channel j [48], $N_j^{\dagger}(E^* - E_{0,j})$ is the sum of ro-vibrational states of the transition state (TS) at an energy ($E^* - E_{0,j}$) above the threshold for channel j, h is Planck's constant, and $\rho(E^*)$ is the density of states of the EM at the available energy, E^*. When the rate of dissociation is much faster than the average experimental time scale, Eq. (4) reduces to Eq. (3). Eq. (4) also accounts for the competition between multiple dissociation pathways using the $k_j(E^*)/k_{tot}(E^*)$ ratio [51, 52]. Calculation of the RRKM unimolecular rate constants in Eq. (5) requires the ro-vibrational states of the EM and TS. The molecular parameters for the EM were taken from quantum chemical calculations of the reactant ion. For water loss, the TS was assumed to be loose with no reverse activation barrier, as the bond cleavage is heterolytic with all the charge remaining on the manganese containing fragment complex [53]. Thus, the water loss TS is product-like and treated in the phase space limit (PSL) [51], such that it uses molecular parameters taken from quantum chemical calculations of the products. Because the charge separation processes produce two singly

charged species, there must be an associated Coulomb barrier along the reaction coordinate for this dissociation channel such that the charge separation TSs are tight. The rate-limiting TSs for charge separation are labeled according to the products formed in reaction (2), i.e., TS[y + (x – y – 1)] where y is the number of water molecules attached to the $MnOH^+$ product and (x – y – 1) is the number of water molecules attached to the H^+ product. Molecular parameters for these TSs were taken directly from the calculations described below.

A sequential dissociation model [54] was employed to simultaneously analyze cross sections for the first and second water losses for a given Mn water complex size. Thresholds for secondary water loss cross sections were modeled with a statistical approach that has been shown to provide accurate thresholds for singly and doubly charged systems [16, 19, 24, 26, 27, 30, 40, 51, 54]. The BDE for the $Mn^{2+}(H_2O)_{x-1}$ complex is the difference between the thresholds of these two product cross sections. The sequential threshold model combines Eq. (4), the cross section of the primary dissociation product, with the probability for further dissociation given by Eq. (6),

$$P_{D2} = 1 - e^{-k_2(E_2^*)\tau} \tag{6}$$

where $k_2(E_2^*)$ is the rate constant for sequential dissociation of a primary product ion having an internal energy of E_2^*. This energy was determined by energy conservation $E_2^* = E^* - E_{0,j} - T_1 - E_L$, where T_1 is the translational energy of the primary products and E_L is the internal energy of the primary neutral product (here, H_2O). As discussed elsewhere, the distributions in these energies are assigned on the basis of statistical considerations [54]. For the remainder of this paper, representation of this sequential dissociation model that combines Eqs. (4) and (6) will be notated as Eq. (4 × 6).

The CID cross section models of Eqs. (4) and (4 × 6) were convolved with the relative kinetic energy distributions of the $Mn^{2+}(H_2O)_x$ and Xe reactants for comparison with the experimental cross sections [31]. A nonlinear least-squares fitting procedure was used to optimize the fitting parameters in each model. The uncertainties associated with the fitting parameters, $\sigma_{0,j}$, n, and $E_{0,j}$, were determined from modeling multiple data sets (at least eight zero pressure extrapolated cross sections for each system) and additional modeling of the cross sections by

scaling the vibrational frequencies by ±10%, varying the best fit n value by ±0.1, scaling the experimental time-of-flight up and down by a factor of 2, and including the absolute uncertainty of the energy scale, ±0.05 eV (Lab). Because all sources of energy are accounted for in these analyses, the measured thresholds, $E_{0,j}$, equal the BDE at 0 K for the $Mn^{2+}(H_2O)_x$ complex dissociating as in reaction (1) [55] or the height of the charge-separation barrier of reaction (2).

Computational Details. Possible geometries for $Mn^{2+}(H_2O)_x$ complexes were taken from previous M^{2+} hydration studies [18, 19, 24-27]. The geometries were optimized at the B3LYP/6-31G(d) level of theory using the Gaussian16 suite of programs [56]. The structures were then refined at a B3LYP/6-311+G(d,p) level [57, 58], where vibrational frequencies and rotational constants were also calculated. Vibrational frequencies were scaled by 0.989 [59] before use in the modeling process or to calculate the zero-point energy and thermal corrections. Single-point energy calculations were performed at B3LYP, B3P86 [60], M06 [61, 62], and MP2(full) [63] levels of theory using a 6-311+G(2d,2p) basis set. The relative energies were calculated from the single point calculations including zero-point corrections to yield 0 K values and thermal corrections to yield 298 K values. Basis set superposition errors (BSSE) were calculated for dissociation of the lowest energy structures at each level of theory in the full counterpoise (cp) limit [64, 65]. In some cases, complexes were also calculated after including empirical dispersion corrections [67, 68] with geometries calculated at the B3LYP-GD3BJ/6-311+G(d,p) level followed by single point energies calculated at B3LYP-GD3BJ level of theory with the 6-311+G(2d,2p) basis set. MP2 single point energies using these geometries were also calculated but yield essentially identical values as those obtained using B3LYP geometries.

We also calculated reaction coordinate diagrams for the dissociations of two complexes at the B3LYP/6-311+G(d,p) level with single point calculations using these geometries and zero-point energy corrections conducted at the B3LYP and MP2(full) levels using the 6-311+G(2d,2p) basis set. All transition states had a single imaginary frequency and connections to intermediates on either side were confirmed by intrinsic reaction coordinate (IRC) calculations.

RESULTS

Collision-Induced Dissociation Cross-Sections of $Mn^{2+}(H_2O)_x$. Experimental cross-sections for the collision-induced dissociation with Xe were acquired for $Mn^{2+}(H_2O)_x$, $x = 4 – 9$, and are shown in Fig. 1. In all cases, the dominant pathway for dissociation is the loss of a single water, reaction (1), followed by loss of additional water molecules as the kinetic energy increases. The total cross section for each complex reaches a plateau and remains constant with increasing energy, consistent with sequential dissociation processes. The magnitude of the total cross section increases as the complex size increases, consistent with the increasing physical size of the complexes. As seen in Fig. 1a – 1e, $x = 5 – 9$, the smallest water loss product observed with ~0.2 mTorr of xenon is $Mn^{2+}(H_2O)_2$. For $x = 4$, $Mn^{2+}(H_2O)$ can also be observed, simply because the smaller reactant complex provides more sensitivity for observing this product.

One unusual feature in the low-energy regions of the cross sections for TCID of $x = 6 – 9$ complexes is the "exothermic" tail observed in the primary products as well as any sequential products having appreciable intensity near zero collision energy. Such features have not been observed in our previous studies of other hydrated metal dications [16-27], although they have been seen previously for hydrated singly-charged metal ions [40]. As in that study, we attribute these barrierless processes to metastable ions, i.e., long-lived ions generated in the source that have sufficient energy to dissociate without the need for adding more energy. In most studies, such energetic ions (associated with the high energy tail in the 300 K Maxwellian distribution formed in the source) dissociate during the time they travel from the source to the collision region, but if their lifetimes are longer than usual, they can be observed. The origins of these metastable species in the Mn^{2+} system are not entirely clear, although we suspect that the high-spin half-filled ^6S ($3d^5$) electron configuration may be a contributing factor.

In addition to loss of water ligands, charge separation (CS) products from reaction (2) were observed for all complexes. The largest $MnOH^+$ complex observed was $MnOH^+(H_2O)_2$ (Fig. 1b – 1f) and the largest hydronium ion observed was $H^+(H_2O)_2$ (Fig. 1a – 1e). In dissociation of

$Mn^{2+}(H_2O)_5$, Fig. 1e, it can be seen that these two products arise from the same threshold, definitively identifying them as coming from the same process, reaction (7).

$$Mn^{2+}(H_2O)_5 \rightarrow MnOH^+(H_2O)_2 + H^+(H_2O)_2 \quad (7)$$

Note that the threshold for this process is well above that for losing a single H_2O ligand from the same reactant complex, explaining why the cross section for reaction (1) is over two orders of magnitude larger. At slightly higher energies in Fig. 1e, the $MnOH^+(H_2O)_2$ cross section continues to increase while the $H^+(H_2O)_2$ cross section plateaus; however, the H^+H_2O product cross section can be observed to nearly match the increase in the $MnOH^+(H_2O)_2$ cross section. Thus, reaction (8) must also be occurring.

$$Mn^{2+}(H_2O)_4 \rightarrow MnOH^+(H_2O)_2 + H^+H_2O \quad (8)$$

It is also possible that formation of H^+H_2O is partially a result of sequential water loss from $H^+(H_2O)_2$, but this process cannot occur until higher energies because $D_0(H^+H_2O\text{-}H_2O) = 1.35 \pm 0.06$ eV [55].

Reaction (8) is more apparent in the dissociation of $Mn^{2+}(H_2O)_4$, Fig. 1f. Here, because reaction (7) cannot occur (explaining why $H^+(H_2O)_2$ is not observed), it is clear that the two singly-charged products of reaction (8) arise from identical thresholds. Furthermore, they have nearly the same energy onset as reaction (1), which is why the magnitudes of the cross sections for reactions (1) and (8) are more similar. Nevertheless, because reaction (8) must pass over a tight Coulomb barrier that is the rate-limiting step in formation of the singly-charged species, the CS processes are entropically disfavored compared to water loss processes that always involve loose transition states. Thus, the cross section for reaction (1) reaches a larger magnitude than that for reaction (8). At higher energies, the $MnOH^+(H_2O)_2$ cross section decreases, consistent with this product losing a water ligand, as shown by the increase in the $MnOH^+H_2O$ cross section.

Note that for both reactions (7) and (8), the hydronium ion products have cross sections that are somewhat smaller than those for the hydrated $MnOH^+$ products, although stoichiometry demands they must be exactly equivalent. We have previously investigated this in detail [19] and

shown that the collection of the hydrated hydronium ion is less efficient because this lighter ion has a higher velocity (due to conservation of linear momentum) than the hydrated metal hydroxide cation. Because energy is released in translational modes as the system passes over the Coulomb barrier, these velocities can be appreciable, making it more difficult to collect the products with 100% efficiency. Focusing conditions can be adjusted to achieve equal collection efficiency but require sacrificing reactant ion intensity; however, these studies show that the cross sections of the metal hydroxide are representative of the absolute cross sections for the CS channels.

The dissociation of $Mn^{2+}(H_2O)_4$ shows two features in the H^+H_2O cross section, Fig. 1f. As noted above, the lower energy feature is attributed to reaction (8), and the higher energy feature can be seen to match the magnitude of the $MnOH^+H_2O$ product ion. This behavior signals a third CS process, reaction (9).

$$Mn^{2+}(H_2O)_3 \rightarrow MnOH^+H_2O + H^+H_2O \quad (9)$$

Here, the threshold for this process occurs well below that for loss of H_2O from $Mn^{2+}(H_2O)_3$, hence the cross section for reaction (9) is larger than that for water loss. Thus, CS is enthalpically and entropically favored over the water loss process for $x = 3$. At the highest energies, the $MnOH^+H_2O$ cross section decreases, which can be attributed to dissociation to form $MnOH^+$, Fig. 1f.

Examination of the CS products in Fig. 1a – 1d shows that they match those observed in Fig. 1e after adjusting for the differences in the required energies. Notably, the $MnOH^+(H_2O)_2$ product is not shown in Fig. 1a because the mass of this product, *m/z* 107.9 cannot be distinguished from that of the much more intense reactant $Mn^{2+}(H_2O)_9$, *m/z* 108.5. For all smaller complexes, this is no longer an issue. Likewise, $MnOH^+H_2O$, *m/z* 89.9, and $Mn^{2+}(H_2O)_7$, *m/z* 90.5, are nearly isobaric, such that the former product cannot be observed in Fig. 1a – 1c, but appears for all smaller complexes.

Overview of Theoretical Results. As described above, the geometry optimizations and vibrational frequency calculations for $Mn^{2+}(H_2O)_x$ (x = 1 - 10) complexes were performed at the B3LYP/6-311+G(d,p) level of theory. For all complexes, the sextet spin state of the $3d^5$

configuration on Mn^{2+} was found to be much more favorable energetically than quartet or doublet spin states. Although experimental data for x = 1 - 3 were not obtained, their optimized structures were calculated for completeness and are presented in the Supporting Information. Relative energies at 0 and 298 K of distinct low-energy isomers of $Mn^{2+}(H_2O)_x$ (x = 3 – 9) complexes calculated at different levels of theory are given in Table 1, with geometries of ground structures (GSs) shown in Fig. 2. A more complete listing of all investigated isomers of $Mn^{2+}(H_2O)_x$ (x = 3 – 10) is provided in the Supporting Information.

To identify different isomers, we use (m, n, p) to describe the number of water molecules in the first (m), second (n), and third (p) solvent shells of each unique structure. To describe the hydrogen bonding of water molecules in the cluster, isomers are further denoted using an A/D nomenclature where a water molecule can be a single (A) or double (AA) hydrogen bond acceptor and/or a single (D) or double (DD) hydrogen bond donor with shells separated by an underscore (_). To further distinguish between structures with similar bonding schemes but differing geometric parameters, the nomenclature may include the subscripts “a” or “b” to indicate if the bond connects to an axial or base ligand, respectively, of an inner shell of five water molecules.

Theoretical geometries for $Mn^{2+}(H_2O)_x$ ground structures. Geometric parameters of optimized ground structures for $Mn^{2+}(H_2O)_x$ are provided in Supporting Information Table S1. All levels of theory predict GSs with water directly binding to the metal dication center for $x \leq 5$. $Mn^{2+}(H_2O)$ has a Mn-O bond length of 1.985 Å, which increases to 1.998 Å in the $Mn^{2+}(H_2O)_2$ complex, where the ∠OMnO bond angle is 180°. Shown in Fig. 2, the (3,0) $Mn^{2+}(H_2O)_3$ GS exhibits a trigonal planar geometry with ∠OMnO of 120°, ∠MnOH of 127° and ∠HOH of 106° with three Mn-O bond lengths of 2.060 Å. The water ligands have a nonsymmetrical orientation (∠HOMnO = 34.5°) because they participate in long-range hydrogen bonding interactions (~3.8 Å between H and O). The (4,0) GS has C_1 symmetry with ∠OMnO of 107° (2) and 111° (4) and four Mn-O bond lengths of 2.108 Å, where the number in parentheses represents the degeneracy. The (3,1)_AA and (3,1)_A isomers promote a water ligand to a second solvent shell, either accepting hydrogen bonds from two inner shell water molecules (AA) or one inner shell water (A).

These isomers lie 42 – 74 kJ/mol higher in energy, Table 1. At 298 K, all levels of theory predict the (3,1)_A isomer is lower in energy than (3,1)_AA, whereas at 0 K, B3LYP and B3P86 finds (3,1)_A is lower in energy and M06 and MP2 find (3,1)_AA is favored. Entropically, the (3,1)_A isomer is favorable because the second shell water can rotate nearly freely, hence the differences between the levels of theory can be attributed to the strength of the hydrogen bonding. For $x = 5$, all levels of theory predict the GS has all water ligands directly binding to the metal center in a square pyramidal geometry having C_{2v} symmetry, Fig. 2. The Mn-O bond lengths are 2.149 (2), 2.150, and 2.201 (2) Å. There are two (4,1) isomers where one water ligand is promoted to the second solvent shell, but these lie 5 – 35 kJ/mol higher in energy, Table 1.

At $Mn^{2+}(H_2O)_6$, all levels of theory predict six water ligands bind directly to the metal center in the GS at 0 K. The (6,0) GS is highly symmetrical with T_h molecular symmetry and uniform Mn-O bond lengths of 2.217 (6) Å and ∠OMnO of 90° (12) and 180° (3). Note that the water molecules are oriented such that there are weak hydrogen bonding interactions with adjacent water molecules (~3.65 Å between H and O). At 298 K, the (6,0) isomers remains the GS at the M06 and MP2 levels of theory, but B3LYP and B3P86 levels predict the (5,1)_A_bA_b isomer is the GS. The (5,1)_A_bA_b isomer has the sixth water ligand accepting hydrogen bonds from two inner solvent shell water ligands in base positions. As shown in Table 1, the (5,1)_A_a isomer is 1 – 2 kJ/mol higher in energy than (5,1)_A_bA_b for B3LYP and B3P86 at 298 K (5 – 7 kJ/mol for M06 and MP2). This isomer has the sixth ligand accepting a single hydrogen bond from the water ligand at the axial position of the inner solvent shell, Fig. 2, such that the outer shell ligand can rotate easily.

The near degeneracy in energy for the (6,0) and (5,1) isomers agrees with the spectroscopic observation by O'Brien and Williams that $Mn^{2+}(H_2O)_6$ changes the number of water ligands from six (at 215 K) to include smaller coordination numbers as the temperature increases to 305 K [66]. Table 2 shows equilibrium population distributions calculated at these two temperatures for the levels of theory considered here. At 215 K, B3LYP and B3P86 incorrectly indicate that the dominant isomers are (5,1), whereas M06 and MP2 indicate the (6,0) isomer dominates. At room

temperature, M06 predicts the (5,1) isomers are too high in energy to contribute, which is not supported by the spectroscopic evidence. MP2 predicts a small population (~4.2%) of (5,1)_A_bA_b, which is most similar to the experimental result but seems low (although the extent of (5,1) population cannot be quantified in the experiments). To further investigate the diverse theoretical results, (6,0) and (5,1) complexes were also calculated after including empirical dispersion corrections as detailed above. According to this level of theory, Table 2, the (6,0) complex dominates at 215 K with 71% of the population, decreasing to 45% at 305 K, with the (5,1) isomers contributing 44%. This latter result seems relatively high compared to the description of the spectroscopic results by O'Brien and Williams. We conclude that MP2 is most accurate out of all the levels considered, but the true relative energies may fall somewhere between MP2 and B3LYP-GD3BJ results. In this context, we have previously found that MP2 calculations are more accurate in predicting the structures found spectroscopically for $Zn^{2+}(H_2O)_x$ complexes than the other levels considered here [69].

For x = 7, 8, and 9, theoretical results diverge from B3LYP and B3P86 to M06 and MP2 at 0 and 298 K. M06 and MP2 uniformly predict six inner-shell water complexes as the GSs at both 0 and 298 K. Outer shell ligands are added such that they each interact with two inner shell ligands (AA), eventually leading to the symmetric (6,3)_6D_3AA complex, Fig. 2. For x = 8, the eighth water ligand can add to an adjacent site (g = gauche orientation), (6,2)_4D_2AA_g (Fig. 2) or across from the first second shell ligand (t = trans orientation), (6,2)_4D_2AA_t. The latter is only higher in energy by 5 – 6 kJ/mol at 0 K and ~ 2 kJ/mol at 298 K. In contrast, B3LYP and B3P86 prefer five-coordinate GSs at 298 K. For $Mn^{2+}(H_2O)_7$, (5,2)_4D_2A_bA_b is the GS at both 0 and 298 K and has the sixth and seventh water ligands accepting hydrogen bonds from two water molecules in base positions of the inner shell opposite one another. For x = 8, the GS at both 0 and 298 K is the (5,3)_4D,DD_2A_bA_b,A_bA_a complex, Fig. 2. For $Mn^{2+}(H_2O)_9$, all four levels of theory predict the six-coordinate structure as the GS at 0 K, but at 298 K, B3LYP and B3P86 predict the five-coordinate structure is lower (although by < 2 kJ/mol). Here, the GS is (5,4)_4DD_4A_bA_b with all four second shell water ligands interacting with two inner water molecules in base

positions. Each inner water ligand is donating to two outer shell water and the second shell water ligands are located equally from the metal center. Spectroscopic results from O'Brien and Williams [69] indicate that the (6, *x*-6) complexes dominate with photodissociation kinetics indicating that Mn^{2+} has "an average CN slightly less than six" at higher temperatures (263 – 331 K). Again, we conclude that MP2 theory is probably providing the best prediction of the relative energetics but destabilizes the (5, *x*-5) structures more than is experimentally realized.

As detailed in Table S1 of the Supporting Information, the Mn-O bond lengths increase from 1.985 Å to 2.217 Å as the complex size increases from one to six water ligands that bind directly to the metal. For the (5,1) complex, the inner shell water molecules bind slightly more tightly than in (6,0), as indicated by Mn-O bond lengths of 2.126 – 2.202 Å. For larger (6,*n*) and (5,*n*) complexes, the inner shell bond lengths remain similar, ranging from 2.191 to 2.242 Å and 2.130 to 2.183 Å, respectively. For these larger complexes, the second solvent shell water ligands have Mn-O bond lengths of 4.007 to 4.080 Å for the (6,*n*) complexes and 3.935 to 3.971 Å for the (5,*n*) complexes.

Theoretical geometries for charge-separation transition states. The transition states (TSs) for the charge-separation reactions (7) – (9) involve the heterolytic cleavage of an O-H bond leading to the incipient products, $MnOH^+(H_2O)_y$ and $H^+(H_2O)_{x-y-1}$. Molecular parameters for these rate-limiting TSs are needed for thermochemical analysis. Optimized geometries of these tight TSs are shown in Fig. 3 with bond lengths and angles provided in Table S2 of the Supporting Information. The (O-H) distances between the incipient products in these TSs are long, between 2.9 and 3.4 Å.

Data Analysis. Primary and secondary dissociation product cross sections for all $Mn^{2+}(H_2O)_x$ complexes observed were modeled in several ways, with average optimum modeling parameters obtained listed in Table 3. It can be seen that the σ_0 values generally match the absolute magnitudes of the cross sections being modeled, with small variations that are tied to the influence of the *n* and E_0 parameters on the model. All complexes are believed to be thermally equilibrated in the source, such that the modeling assumes the reactant isomers are the 298 K GS with an

internal energy distribution of 298 K. The product isomer is assigned as the 0 K GS because previous studies have found that the threshold analyses are dominated by the lowest energy 0 K enthalpy species [18]. As noted above, the predicted GSs differ for the x = 6 – 9 complexes depending on the level of the theory, and in several cases, there are low-energy isomers at 298 K such that multiple isomers could be present in the source. For each possible GS, the data were modeled individually using each of these possible isomers, Table 3.

Threshold E_0 values were determined for the primary dissociation of each complex from modeling with and without including RRKM theory, which takes lifetime effects into account. The primary threshold values without lifetime effects are larger than those including lifetime effects by 0.08 – 0.27 eV. For x = 6 – 9, these kinetic shifts gradually increase as the complexes get larger because of the increased number of degrees of freedom. For x = 4 and 5, the lifetime effects have the largest threshold changes (0.27 and 0.16 eV, respectively), a consequence of the added complexities associated with the competing CS channels for these two systems. Table 3 also includes values of entropies of activation, $\Delta S^{\dagger}_{1000}$, which represent the looseness of the TSs. All of the values for water loss are positive, consistent with loose PSL TSs. Those for the CS TSs are also positive, a reflection of the floppiness of these structures, Fig. 3.

Fig. 4 shows a typical example of the modeling of the total cross section (which is identical to that obtained for the sequential model shown, as discussed further below). As noted above, for most complex sizes, dissociation of metastable intermediates was observed at low energies. Therefore, in contrast to most systems we have studied, reactant species whose Maxwellian internal energy distribution included populations exceeding the threshold for dissociation were not truncated from the reactants. As shown in Fig. 4, this permits reasonable reproduction of the "exothermic tails" in these cross sections. Notably, the model shows a larger tail than the experiment. Because the model assumes *all* metastable ions survive to enter the collision cell, this comparison demonstrates that some of these metastable ions dissociate during their flight time from the ion source.

Thermochemical results for competitive water loss *versus* charge separation. For $Mn^{2+}(H_2O)_4$ and $Mn^{2+}(H_2O)_5$, water loss and charge-separation processes are competitive primary dissociation pathways, as shown in Fig. 1e and 1f. These dissociative pathways are modeled simultaneously using Eq. (4) with optimum modeling parameters also included in Table 3. The measured E_0 values for water loss are essentially unaffected by including the competition with the CS products. Competitive analysis of the $x = 5$ cross sections measures a dissociation threshold for a single water molecule loss of 1.12 ± 0.07 eV and a threshold for TS[2+2] of 1.40 ± 0.07 eV, such that reaction (1) is energetically favored by 0.28 ± 0.03 eV compared to the CS reaction (7). A competitive pathway analysis for $Mn^{2+}(H_2O)_4$ yields a threshold for water loss of 1.77 ± 0.06 eV and for CS over TS[2+1] of 1.48 ± 0.08 eV. Here, the CS reaction (8) is favored over reaction (1) by 0.29 ± 0.03 eV. As a consequence, in-source fragmentation of the $x = 4$ complex will no longer form smaller $Mn^{2+}(H_2O)_x$ complexes, as observed experimentally.

Thermochemical results for sequential dissociation. Thermochemical results for the secondary water loss thresholds using the sequential model for analysis are also reported in Table 3. The sequential secondary water losses were modeled by simultaneously analyzing the primary and secondary dissociation product cross-sections using Eqs. (4) and (4 × 6), where the difference between the primary and secondary thresholds is an independent measurement of the BDE for $Mn^{2+}(H_2O)_{x-1}$ dissociating to $Mn^{2+}(H_2O)_{x-2} + H_2O$. This difference in thresholds can be measured with more precision than the absolute values for each threshold because many systematic sources of uncertainty cancel; however, their accuracy can suffer from the additional assumptions needed in the modeling [54]. As shown by the example in Fig. 4, both product cross sections and their total are reproduced well over extended magnitudes and energy ranges (~ 2 eV) in the sequential analysis. Direct comparison of the models for the total cross section *versus* the sequential models of the primary water loss cross sections show that the analogous σ_0, n, and E_0 values nearly match. Thus, threshold energies for the primary water loss channels are largely unaffected by consideration of the secondary water loss channel.

The sequential dissociation at $x = 5$ is modeled as the (5,0) → (4,0) + H_2O → (3,0) + $2H_2O$ process; however, these dissociations compete with the CS reactions (7) and (8). Thus, the sequential process was analyzed including competition with the CS products and the results are shown in Fig. 5. Thresholds measured are 1.12 ± 0.07 and 2.87 ± 0.14 eV for the first and second water loss, respectively, with a difference between the thresholds of 1.75 ± 0.07 eV, equal to $D_0[Mn^{2+}(H_2O)_3\text{-}H_2O]$. This value is within the experimental uncertainties of the threshold for the primary water loss channel from $Mn^{2+}(H_2O)_4$, 1.77 ± 0.06 eV. For the competitive CS processes, the barrier height measured for TS[2+1] is 2.70 ± 0.15 eV, 1.58 ± 0.08 eV above the primary water loss threshold. This value is comparable with the barrier height of TS[2+1], 1.48 ± 0.08 eV, found by analyzing the primary dissociations of $Mn^{2+}(H_2O)_4$.

The sequential dissociation at $x = 4$ is similar to $x = 5$ and is modeled as (4,0) → (3,0) + H_2O → (2,0) + $2H_2O$ processes. Again, these water loss dissociations compete with the CS processes of reactions (8) and (9). The sequential process was analyzed including competition with the CS products and the thresholds measured are 1.77 ± 0.06 and 3.90 ± 0.06 eV for the first and second water loss for $x = 4$, respectively. The difference between the thresholds is 2.12 ± 0.04 eV, which provides the BDE of $Mn^{2+}(H_2O)_3$. For the secondary CS process forming $MnOH^+H_2O$ + H^+H_2O, the threshold is measured as 3.24 ± 0.04 eV, 1.47 ± 0.03 eV above the threshold for primary water loss. This value is the barrier height of TS[1+1] and lies 0.67 ± 0.05 eV lower than the secondary water loss channel. Thus, as for $x = 4$, the CS process from $x = 3$ is energetically favored compared to water loss.

Conversion of 0 K hydration energies to 298 K values. In all cases, the threshold energies obtained including lifetime effects are assigned as the 0 K BDEs. To convert to 298 K bond enthalpies (ΔH_{298}) and Gibbs energies (ΔG_{298}) of dissociation, a rigid rotor/harmonic oscillator (RR/HO) approximation using vibrational frequencies (scaled by 0.989) and rotational constants calculated at the B3LYP/6-311+G(d,p) level of theory was used to determine ΔH_{298}-ΔH_0 and $T\Delta S_{298}$ values for dissociation, Table 4. The uncertainties in the conversion factors were obtained by scaling the vibrational frequencies up and down by 10%. Limitations in these

conversions include the fact that some of the low vibrational frequencies that correspond to torsional motions may not be accurate. Further, the accuracy of these frequencies for tight transition states is not as well calibrated as for stable molecules. The 298 K hydration enthalpies (ΔH_{298}) track the trends from the 0 K hydration energies (ΔH_0) discussed below. The Gibbs energies of dissociation (ΔG_{298}) decrease with increasing number of water ligands for all complexes observed.

DISCUSSION

Comparison of primary and secondary experimental bond energies. Primary and secondary experimental hydration enthalpies at 0 K for the loss of water from $Mn^{2+}(H_2O)_x$ (x = 3 - 9) complexes are compared in Table 5. In previous spectroscopic and theoretical work on the hydration of Zn^{2+} [69], the most accurate interpretations of the data were from relative energies and GSs predicted at the MP2 level of theory. As discussed above, the same appears to be true for Mn^{2+} as well. Therefore, Table 5 lists BDEs from MP2 predicted GSs except for x = 6 where (5,1) is included because spectroscopic experiments [69] suggest its presence at 298 K. (Notably, GSs predicted by other levels of theory have experimental BDEs that are within 5 kJ/mol, so the final experimental values are not sensitive to which GS is assumed.) Secondary BDEs obtained from the difference between the primary and secondary thresholds agree fairly well with the corresponding primary BDEs, but are generally higher. The only exception is x = 4, where the threshold energy from the primary analysis is ~ 6 kJ/mol higher but within the combined uncertainties of the sequential threshold energy. Overall, the mean absolute deviation (MAD) between the primary and secondary values is 12 ± 4 kJ/mol, which is somewhat larger than the mean experimental uncertainties of either set of values. Such differences are comparable to those obtained for other metal systems, including $Mg^{2+}(H_2O)_x$ (7 kJ/mol), $Ca^{2+}(H_2O)_x$ (12 kJ/mol), $Sr^{2+}(H_2O)_x$ (7 kJ/mol), $Ba^{2+}(H_2O)_x$ (16 kJ/mol), $Cd^{2+}(H_2O)_x$ (7 kJ/mol), $Fe^{2+}(H_2O)_x$ (4 kJ/mol), $Co^{2+}(H_2O)_x$ (8 kJ/mol), and $Ni^{2+}(H_2O)_x$ (23 kJ/mol) complexes [16, 20-22, 24-26, 70].

The largest discrepancy between the primary and secondary threshold energies is found for $x = 6$ (17.7 kJ/mol). It is possible this is because the two measurements actually refer to different isomers. As noted above, the analysis of the primary BDE for $x = 6$ assumes that the complex has the 298 K structure, which could be either (6,0) according to M06 and MP2 theory, (5,1) according to B3LYP and B3P86 theory, or isoenergetic according to B3LYP-GD3BJ. In contrast, the secondary BDE for $x = 6$ comes from the decomposition of (6,1), which should dissociate to (6,0), the 0 K GS at all levels of theory, and then to (5,0). The assignment of these BDEs is discussed further in the next section.

Trends in the primary and secondary experimental $Mn^{2+}(H_2O)_x$ BDEs are shown in Fig. 6. In general, as the complex size increases from $Mn^{2+}(H_2O)_3$ to $Mn^{2+}(H_2O)_9$, the hydration energies decrease. BDEs decrease rapidly from $x = 3$ to 7, whereas for $x = 7 – 9$, the BDEs are fairly similar (within 4 kJ/mol). The latter result is consistent with putting the $7^{th} – 9^{th}$ ligands in the second solvent shell with similar binding, Fig. 2.

Comparison of experimental and theoretical bond energies. Table 5 also includes theoretical 0 K hydration BDEs for the loss of water from $Mn^{2+}(H_2O)_x$ ($x = 1 – 9$) complexes with and without counterpoise (cp) corrections. The counterpoise corrected values are shown in Fig. 6. Our experimental values agree well with calculated 0 K hydration enthalpies at the B3LYP, B3P86, and MP2 levels of theory, with MADs of 4 – 6 kJ/mol for primary BDEs and 6 – 8 kJ/mol for the secondary BDEs. M06 predicts higher BDEs than the other methods for all complex sizes except $x = 1$ and 2, and as a result has greater deviations from the experimental values, 16 and 10, respectively. When the cp correction is not included, the agreement with primary experimental BDEs worsens for all levels of theory.

For $x = 3$ and 4, the B3LYP, B3P86, and MP2 levels of theory agree with the experimental values relatively well for both primary and secondary BDEs. The primary BDE for $x = 5$ agrees with B3LYP, B3P86, and MP2 within experimental uncertainty. For $x = 6$, it can be seen that the primary BDE does not change appreciably whether the data are interpreted as the (5,1) or the (6,0) complex, 85.9 and 87.8 kJ/mol, respectively. Both of these values agree well with the calculated

BDEs for the (5,1)_A_bA_b complex at all levels of theory, and also with the (6,0) complex for the B3LYP and B3P86 approaches. Likewise, the B3LYP-GD3BJ approach finds BDEs of 86.3 and 87.9 kJ/mol, respectively, also in agreement with the primary experimental BDEs. In contrast, the secondary BDE of 105.5 ± 2.5 kJ/mol agrees nicely with the MP2 value for the (6,0) complex, 101.7 kJ/mol. As noted above, the MP2 approach predicts relative energies of the (6,0) and (5,1) complexes that agree better with the spectroscopic observations of O'Brien and Williams. Thus, as discussed above, it is plausible that the primary BDE corresponds to (5,1), while the secondary BDE can be associated with (6,0).

For larger complexes, x = 7 – 9, the primary BDEs are overestimated by 1 – 9 kJ/mol for B3LYP, 5 – 7 for B3P86, and 1 – 5 for MP2 levels, with M06 too large by 7 – 12 kJ/mol. All levels of theory lie below the secondary BDEs for x = 7 and 8, which could suggest that these experimental values may be too high. For x = 7 and 8, O'Brien and Williams saw evidence for (5, x-5) structures and concluded the average coordination number was slightly less than 6. As noted above, this observation indicates that the (6, x-6) complexes must be the GSs but that some (5, x-5) complexes may be present in the ion beams formed at 298 K. A small contribution of the less stable (5, x-5) complexes may explain the slightly lower experimental primary BDEs compared to the theoretical results.

Overall, B3LYP, B3P86, and MP2 levels of theory provide comparable reproduction of the experimental values for both primary and secondary BDEs, with mean absolute deviations (MADs) of < 6 and < 8 kJ/mol, respectively, whereas M06 is generally too high. Notably, if the primary and secondary BDEs for x = 6 are assigned to (5,1) and (6,0), respectively, the MAD for MP2 calculations declines from 5.9 to 4.0 kJ/mol, whereas those for B3LYP and B3P86 remain the same within 0.2 kJ/mol.

Charge separation: energetic barriers. Table 6 presents the barrier heights measured and calculated for the charge separation (CS) processes of $Mn^{2+}(H_2O)_x$, where x = 3 – 5, and compares them with the experimental and predicted energies for water loss dissociation pathways. The likely rate-limiting TS structures for CS are shown in Fig. 3, and in each case, correspond to heterolytic

cleavage of an O-H bond. For the (3,0) complex, the water loss dissociation pathway is predicted to be 201 – 215 kJ/mol, in good agreement with the experimental value of 205 ± 3 kJ/mol. The CS process, reaction (9), has an experimental threshold of 140 ± 4 kJ/mol. This value lies somewhat above the calculated barrier heights of TS[1+1], although the M06 and MP2 values of 117 and 118 kJ/mol are in reasonable agreement. Certainly, theory correctly predicts that TS[1+1] is much lower in energy than the water loss channel (by 83 – 109 kJ/mol), whereas experiment obtains a difference of only 65 ± 5 kJ/mol. Theory also predicts that the $MnOH^+H_2O + H^+H_2O$ products lie 54 – 87 kJ/mol below the $Mn^{2+}(H_2O)_3$ reactant.

For $x = 4$, the CS process is reaction (8), where $Mn^{2+}(H_2O)_4$ dissociates into $MnOH^+(H_2O)_2 + H^+H_2O$ via TS[2+1]. Here, B3LYP and B3P86 levels predict TS energies within experimental uncertainty and also closely agree with the experimental value for the water loss pathway. As for TS[1+1], M06 and MP2 yield TS energies about 20 kJ/mol above those for B3LYP and B3P86. The barrier height of TS[2+1] is 1 – 27 kJ/mol lower than the water loss dissociation pathway according to theory, compared with an experimental difference of 28 ± 10 kJ/mol. We also mapped out the reaction coordinates for this CS pathway, as shown in Fig. 7. The (4,0) GS requires movement of one water ligand to the second solvent shell to form the (3,1)_A complex. Cleavage of an OH bond in this complex leads to TS[2+1] which dissociates into $MnOH^+(H_2O)_2$ and H^+H_2O. These products lie 3 – 25 kJ/mol below the reactant complex according to DFT and 6 kJ/mol above according to MP2, Table 6.

The CS channel of $Mn^{2+}(H_2O)_5$ forms $MnOH^+(H_2O)_2 + H^+(H_2O)_2$ in reaction (7) via TS[2+2]. B3LYP and B3P86 predict this TS lies near 90 kJ/mol, well below the experimental value of 135 ± 7 kJ/mol, whereas M06 and MP2 predict higher barriers, in reasonable agreement with experiment. In addition, B3LYP and B3P86 predict that water loss occurs at higher energies than the CS reaction (7), whereas M06 and MP2 predict the reverse, which agrees with experimental observation. Overall, formation of the final products in the CS reaction (7) is exothermic, with DFT levels of theory predicting the reaction to be more exothermic than the M06 and MP2 by 42 – 50 kJ/mol. To investigate this CS process further, a complete reaction coordinate

for the decomposition of $Mn^{2+}(H_2O)_5$ was investigated theoretically, as shown in Fig. 8. (It can be noted that the pathway shown here may not be unique.) The (5,0) GS of $x = 5$ moves one water ligand into the second solvent shell to form the (4,1)_AA complex, which then rearranges into (3,2)_3D_AA,A when another water ligand moves to the second solvent shell. This second shell water then transfers to form (3,2)_D,DD_AA,A, where the complex can rearrange further into (3,1,1)_AAD_A and (3,1,1)_AD_A complexes. The latter complex is the obvious precursor to TS[2+2]. Notably, B3LYP and B3P86 levels of theory predict that the barrier height of TS[(3,2)-(3,1,1)] is higher than TS[2+2] by 5 – 6 kJ/mol, whereas M06 and MP2 predict the opposite by 8 – 20 kJ/mol. All four levels of theory have the TS[(3,2)-(3,1,1)] barrier height lower than the water loss pathway, such that B3LYP and B3P86 still predict the CS barrier height is lower than that for water loss. Hence, M06 and MP2 levels of theory more accurately represent the experimental behavior, with MP2 reproducing the experimental values of both pathways the best, Table 6.

As discussed above and seen in Fig. 1, the experimental cross sections show that CS occurs for $Mn^{2+}(H_2O)_x$, where $x = 3 – 5$. From earlier definitions of critical size, the maximum value of x at which CS is competitive with the simple water loss, x_{crit} for $Mn^{2+}(H_2O)_x$ would be 5; however, our competitive analysis shows that the CS process is energetically disfavored over water loss for $x = 5$. Using the energy-dependent definition of the critical size [18], the largest value of x at which CS is energetically favored over the loss of a water ligand, x_{crit} for $Mn^{2+}(H_2O)_x$ is 4, Table 6. This x_{crit} value for Mn^{2+} agrees with that suggested by Shvartsburg and Siu [15] but differs from the $x_{crit} = 3$ value of Kebarle and co-workers [5, 6, 12]. In both reports, their experimental observations do not allow the $MnOH^+(H_2O)_y$ and $H^+(H_2O)_{x-y-1}$ products to be linked to each other nor to the corresponding reactants; therefore, it is difficult to definitively determine the operative reaction pathways in those studies.

CONCLUSION

The kinetic energy dependent cross sections for collision-induced dissociation of $Mn^{2+}(H_2O)_x$ complexes, where $x = 4 – 9$, were determined using guided ion beam tandem mass

spectrometry to complement previous studies of the hydration of late 3d transition metal dications [18, 19, 24-27]. The dominant CID pathway for all complexes studied is the loss of a single water ligand from the reactant ion. The kinetic energy dependent cross sections were analyzed to determine the primary and secondary bond dissociation energies (BDEs) for losing one and two water molecules from the reactant complexes. The BDEs decrease significantly from $x = 3 – 5$, where the water ligands are directly bound to the metal center, whereas BDEs for $x = 7 – 9$ complexes are similar to each other, consistent with water ligands being lost from the second solvent shells in comparable binding motifs. For $x = 6$, previous spectroscopic evidence suggests both (6,0) and (5,1) complexes are present at room temperature, such that the primary threshold may be assigned to the (5,1) complex, whereas the secondary threshold is almost certainly the (6,0) complex. Theoretical calculations of these hydration energies gave reasonable agreement with the experimental primary and secondary BDEs within their uncertainties. MP2 theory more accurately describes the relative energies of the $x = 6$ complexes compared to the DFT approaches and yields the best reproduction of the primary and secondary thresholds for this complex as well.

CS processes are observed for $x = 3 – 5$ complexes and involve Coulomb barriers to form the pair of singly charged products. Accurate analysis of these complexes requires consideration of the competition between water loss and the CS reactions and allows quantitative measurement of the Coulomb barriers for all three CS processes observed. Using the energy dependent definition of x_{crit}, we definitively determine the critical complex size is 4, which agrees with M06 and MP2 theory, but not with B3LYP and B3P86.

Acknowledgement

Financial support was provided by the National Science Foundation, Grant No. 1954142. The Center for High Performance Computing (CHPC) at the University of Utah is acknowledged for their generous allocation of computing time. We are pleased to publish this paper in honor of Paul Kebarle’s many contributions to thermodynamics and ion chemistry, in particular, his seminal measurements of hydration energies.

References

[1] J. Emsley, Nature's building blocks: an AZ guide to the elements, Oxford University Press, 2011.
[2] M. Aschner, K.M. Erikson, E.H. Hernández, R. Tjalkens, Manganese and its role in Parkinson's disease: from transport to neuropathology, NeuroMol. Med., 11 (2009) 252-266.
[3] S.K. Searles, P. Kebarle, Hydration of the Potassium Ion in the Gas Phase: Enthalpies and Entropies of Hydration Reactions $K^+(H_2O)_{n-1} + H_2O = K^+(H_2O)_n$ for n = 1 to n = 6, Can. J. Chem., 47 (1969) 2619-2627.
[4] I. Dzidic, P. Kebarle, Hydration of the alkali ions in the gas phase. Enthalpies and entropies of reactions $M^+(H_2O)_{n-1} + H_2O = M^+(H_2O)_n$, J. Phys. Chem., 74 (1970) 1466-1474.
[5] A.T. Blades, P. Jayaweera, M.G. Ikonomou, P. Kebarle, Ion-molecule Clusters Involving Doubly Charged Metal Ions (M^{2+}), Int. J. Mass Spectrom., 102 (1990) 251-267.
[6] A.T. Blades, P. Jayaweera, M.G. Ikonomou, P. Kebarle, Studies of Alkaline Earth and Transition Metal M^{++} Gas Phase Ion Chemistry, J. Chem. Phys., 92 (1990) 5900-5906.
[7] M. Peschke, A.T. Blades, P. Kebarle, Hydration Energies and Entropies for Mg^{2+}, Ca^{2+}, Sr^{2+}, and Ba^{2+} from Gas-phase Ion-water Molecule Equilibria Determinations, J. Phys. Chem. A, 102 (1998) 9978-9985.
[8] M. Peschke, A.T. Blades, P. Kebarle, Formation, acidity and charge reduction of the hydrates of doubly charged ions M^{2+} (Be^{2+}, Mg^{2+}, Ca^{2+}, Zn^{2+}), Int. J. Mass Spectrom., 185/186/187 (1999) 685–699.
[9] M. Peschke, A.T. Blades, P. Kebarle, Binding energies for doubly-charged ions $M^{2+} = Mg^{2+}$, Ca^{2+} and Zn^{2+} with the ligands L = H_2O, acetone and N-methylacetamide in complexes ML_n^{2+} for n = 1 - 7 from gas phase equilibra determinations and theoretical calculations, J. Am. Chem. Soc., 122 (2000) 10440-10449.
[10] W.A. Donald, R.D. Leib, M. Demireva, B. Negru, D.M. Neumark, E.R. Williams, Average Sequential Water Molecule Binding Enthalpies of $M(H_2O)_{19-124}^{2+}$ (M = Co, Fe, Mn, and Cu) Measured with Ultraviolet Photodissociation at 193 and 248 nm, J. Phys. Chem. A, 115 (2011) 2-12.
[11] S.E. Rodriguez-Cruz, R.A. Jockusch, E.R. Williams, Hydration Energies of Divalent Metal Ions, $Ca^{2+}(H_2O)_n$ (n = 5-7) and $Ni^{2+}(H_2O)_n$ (n = 6-8), Obtained by Blackbody Infrared Radiative Dissociation, J. Am. Chem. Soc., 120 (1998) 5842-5843.
[12] P. Jayaweera, A.T. Blades, M.G. Ikonomou, P. Kebarle, Production and study in the gas phase of multiply charged solvated or coordinated metal ions, J. Am. Chem. Soc., 112 (1990) 2452-2454.
[13] Z.L. Cheng, K.W.M. Siu, R. Guevremont, S.S. Berman, Electrospray Mass Spectrometry: A Study on Some Aqueous Solutions of Metal Salts, J. Am. Soc. Mass Spectrom., 3 (1992) 281-288.
[14] S.G. Anderson, A.T. Blades, J. Klassen, P. Kebarle, Determination of Ion-Ligand Bond Energies and Ion Fragmentation Energies of Electrospray-Produced Ions by Collision-Induced Dissociation Threshold Measurements, Int. J. Mass Spectrom. Ion Processes, 141 (1995) 217-228.
[15] A.A. Shvartsburg, K.W.M. Siu, Is There a Minimum Size for Aqueous Doubly Charged Metal Cations?, J. Am. Chem. Soc., 123 (2001) 10071-10075.
[16] T.E. Cooper, P.B. Armentrout, Sequential Bond Energies and Barrier Heights for the Water Loss and Charge Separation Dissociation Pathways of $Cd^{2+}(H_2O)_n$, n = 3-11, J. Chem. Phys., 134 (2011) 114308.

[17] T.E. Cooper, P.B. Armentrout, Threshold Collision-induced Dissociation of Hydrated Cadmium (II): Experimental and Theoretical Investigation of the Binding Energies for $Cd^{2+}(H_2O)_n$ Complexes (n = 4 – 11), Chem. Phys. Lett., 486 (2010) 1-6.
[18] T.E. Cooper, D.R. Carl, P.B. Armentrout, Hydration Energies of Zinc (II): Threshold Collision-induced Dissociation Experiments and Theoretical Studies, J. Phys. Chem. A, 113 (2009) 13727–13741.
[19] T.E. Cooper, P.B. Armentrout, Experimental and Theoretical Investigation of the Charge-Separation Energies of Hydrated Zinc(II): Redefinition of the Critical Size, J. Phys. Chem. A, 113 (2009) 13742-13751.
[20] O.W. Wheeler, D.R. Carl, T.E. Hofstetter, P.B. Armentrout, Hydration Enthalpies of $Ba^{2+}(H_2O)_x$, x = 1 – 8: A Threshold Collision-Induced Dissociation and Computational Investigation, J. Phys. Chem. A, 119 (2015) 3800-3815.
[21] D.R. Carl, P.B. Armentrout, Experimental Investigation of the Complete Inner Shell Hydration Energies of Ca^{2+}: Threshold Collision-induced Dissociation of $Ca^{2+}(H_2O)_x$ Complexes (x = 2 – 8), J. Phys. Chem. A, 116 (2012) 3802-3815.
[22] D.R. Carl, P.B. Armentrout, Threshold Collision-Induced Dissociation of Hydrated Magnesium: Experimental and Theoretical Investigation of the Binding Energies for $Mg^{2+}(H_2O)_x$ complexes (x = 2 – 10), ChemPhysChem, 14 (2013) 681-697.
[23] D.R. Carl, B.K. Chatterjee, P.B. Armentrout, Threshold Collision-induced Dissociation of $Sr^{2+}(H_2O)_x$ Complexes (x = 1 – 6): An Experimental and Theoretical Investigation of the Complete Inner Shell Hydration Energies of Sr^{2+}, J. Chem. Phys., 132 (2010) 044303.
[24] T.E. Hofstetter, P.B. Armentrout, Threshold Collision-Induced Dissociation and Theoretical Studies of Hydrated Fe(II): Binding Energies and Coulombic Barrier Heights, J. Phys. Chem. A, 117 (2013) 1110-1123.
[25] R.A. Coates, P.B. Armentrout, Binding Energies of Hydrated Cobalt(II) by Collision-Induced Dissociation and Theoretical Studies: Evidence for a New Critical Size, Phys. Chem. Chem. Phys., 20 (2018) 802-818.
[26] R.A. Coates, P.B. Armentrout, Thermochemical Investigations of Hydrated Nickel Dications Complexes by Threshold Collision-Induced Dissociation and Density Functional Theory, J. Phys. Chem. A, 121 (2017) 3629-3646.
[27] A.F. Sweeney, P.B. Armentrout, Hydrated Copper Ion Chemistry: Guided Ion Beam and Computational Investigation of $Cu^{2+}(H_2O)_n$ (n = 7 – 10) Complexes, Eur. J. Mass Spectrom., 21 (2015) 497-516.
[28] O. Sander, P.B. Armentrout, Hydration Energies of Iron Hydroxide Cation: A Guided Ion Beam and Theoretical Investigation, J. Phys. Chem. A, 123 (2019) 1675-1688.
[29] R.A. Coates, P.B. Armentrout, Binding Energies of Hydrated Cobalt Hydroxide Ion Complexes: A Guided Ion Beam and Theoretical Investigation, J. Chem. Phys., 147 (2017) 064305.
[30] A.F. Sweeney, P.B. Armentrout, Guided Ion Beam Studies of the Collision-induced Dissociation of $CuOH^+(H_2O)_n$ (n = 1-4): Comprehensive Thermodynamic Data for Copper Ion Hydration, J. Phys. Chem. A, 118 (2014) 10210-10222.
[31] K.M. Ervin, P.B. Armentrout, Translational Energy Dependence of $Ar^+ + XY \rightarrow ArX^+ + Y$ (XY = H_2, D_2, HD) from Thermal to 30 eV c.m., J. Chem. Phys., 83 (1985) 166-189.
[32] F. Muntean, P.B. Armentrout, Guided Ion Beam Study of Collision-Induced Dissociation Dynamics: Integral and Differential Cross Sections, J. Chem. Phys., 115 (2001) 1213-1228.

[33] R.M. Moision, P.B. Armentrout, An Electrospray Ionization Source for Thermochemical Investigation with the Guided Ion Beam Mass Spectrometer, J. Am. Soc. Mass Spectrom., 18 (2007) 1124-1134.
[34] S.A. Shaffer, D.C. Prior, G.A. Anderson, H.R. Udseth, R.D. Smith, An Ion Funnel Interface for Improved Ion Focusing and Sensitivity Using Electrospray Ionization Mass Spectrometry, Anal. Chem., 70 (1998) 4111-4119.
[35] D.R. Carl, R.M. Moision, P.B. Armentrout, In-source Fragmentation Technique for the Production of Thermalized Ions, J. Am. Soc. Mass Spectrom., 20 (2009) 2312-2317.
[36] J.E. Carpenter, C.P. McNary, A. Furin, A.F. Sweeney, P.B. Armentrout, How Hot are Your Ions Really? A Threshold Collision-Induced Dissociation Study of Substituted Benzylpyridinium "Thermometer" Ions, J. Am. Soc. Mass Spectrom., 28 (2017) 1876-1888.
[37] S.J. Ye, P.B. Armentrout, Absolute Thermodynamic Measurements of Alkali Metal Cation Interactions with a Simple Dipeptide and Tripeptide, J. Phys. Chem. A, 112 (2008) 3587-3596.
[38] D. Gerlich, Inhomogeneous rf Fields: A Versatile Tool for the Study of Processes with Slow Ions, in: C.-Y. Ng, M. Baer (Eds.) Adv. Chem. Phys., 1992, pp. 1-176.
[39] N. Aristov, P.B. Armentrout, Collision-Induced Dissociation of Vanadium Monoxide Ion, J. Phys. Chem., 90 (1986) 5135-5140.
[40] N.F. Dalleska, K. Honma, L.S. Sunderlin, P.B. Armentrout, Solvation of Transition Metal Ions by Water. Sequential Binding Energies of $M^+(H_2O)_x$ (x = 1 - 4) for M = Ti - Cu Determined by Collision-Induced Dissociation, J. Am. Chem. Soc., 116 (1994) 3519-3528.
[41] D.A. Hales, P.B. Armentrout, Effect of Internal Excitation on the Collision-Induced Dissociation and Reactivity of Co_2^+, J. Cluster Science, 1 (1990) 127-142.
[42] N.R. Daly, Scintillation Type Mass Spectrometer Ion Detector, Rev. Sci. Instrum., 31 (1960) 264-267.
[43] D.A. Hales, L. Lian, P.B. Armentrout, Collision-Induced Dissociation of Nb_n^+ (n = 2 - 11): Bond Energies and Dissociation Pathways, Int. J. Mass Spectrom. Ion Processes, 102 (1990) 269-301.
[44] R.H. Schultz, P.B. Armentrout, Threshold Collisional Activation of $Fe^+ \cdot C_3H_8$: Probing the Potential Energy Surface, J. Am. Chem. Soc., 113 (1991) 729-730.
[45] T.S. Beyer, D.F. Swinehart, Number of Multiply-Restricted Partitions, Commun. ACM, 16 (1973) 379.
[46] S.E. Stein, B.S. Rabinovich, On the Use of Exact State Counting Methods in RRKM Rate Calculations, Chem. Phys. Lett., 49 (1977) 183-188.
[47] S.E. Stein, B.S. Rabinovitch, Accurate Evaluation of Internal Energy Level Sums and Densities Including Anharmonic Oscillators and Hindered Rotors, J. Chem. Phys., 58 (1973) 2438-2445.
[48] R.G. Gilbert, S.C. Smith, Theory of Unimolecular and Recombination Reactions, Blackwell Scientific, London, 1990.
[49] K.A. Holbrook, M.J. Pilling, S.H. Robertson, Unimolecular Reactions, 2nd ed., Wiley, New York, 1996.
[50] D.G. Truhlar, B.C. Garrett, S.J. Klippenstein, Current Status of Transition-State Theory, J. Phys. Chem., 100 (1996) 12771-12800.
[51] M.T. Rodgers, K.M. Ervin, P.B. Armentrout, Statistical Modeling of Collision-Induced Dissociation Thresholds, J. Chem. Phys., 106 (1997) 4499-4508.
[52] M.T. Rodgers, P.B. Armentrout, Statistical Modeling of Competitive Threshold Collision-Induced Dissociation, J. Chem. Phys., 109 (1998) 1787-1800.

[53] P.B. Armentrout, J. Simons, Understanding Heterolytic Bond Cleavage, J. Am. Chem. Soc., 114 (1992) 8627-8633.
[54] P.B. Armentrout, Statistical modeling of sequential collision-induced dissociation, J. Chem. Phys., 126 (2007) 234302.
[55] N.F. Dalleska, K. Honma, P.B. Armentrout, Stepwise Solvation Enthalpies of Protonated Water Clusters: Collision Induced Dissociation as an Alternative to Equilibrium Studies, J. Am. Chem. Soc., 115 (1993) 12125-12131.
[56] M.J. Frisch, G.W. Trucks, H.B. Schlegel, G.E. Scuseria, M.A. Robb, J.R. Cheeseman, G. Scalmani, V. Barone, G.A. Petersson, H. Nakatsuji, X. Li, M. Caricato, A.V. Marenich, J. Bloino, B.G. Janesko, R. Gomperts, B. Mennucci, H.P. Hratchian, J.V. Ortiz, A.F. Izmaylov, J.L. Sonnenberg, D. Williams-Young, F. Ding, F. Lipparini, F. Egidi, J. Goings, B. Peng, A. Petrone, T. Henderson, D. Ranasinghe, V.G. Zakrzewski, J. Gao, N. Rega, G. Zheng, W. Liang, M. Hada, M. Ehara, K. Toyota, R. Fukuda, J. Hasegawa, M. Ishida, T. Nakajima, Y. Honda, O. Kitao, H. Nakai, T. Vreven, K. Throssell, J. J. A. Montgomery, J.E. Peralta, F. Ogliaro, M.J. Bearpark, J.J. Heyd, E.N. Brothers, K.N. Kudin, V.N. Staroverov, T.A. Keith, R. Kobayashi, J. Normand, K. Raghavachari, A.P. Rendell, J.C. Burant, S.S. Iyengar, J. Tomasi, M. Cossi, J.M. Millam, M. Klene, C. Adamo, R. Cammi, J.W. Ochterski, R.L. Martin, K. Morokuma, O. Farkas, J.B. Foresman, D.J. Fox, Gaussian 16, Revision A.03, in, Gaussian, Inc., Wallingford CT, 2016.
[57] A.D. Becke, Density-functional Thermochemistry. III. The Role of Exact Exchange, J. Chem. Phys., 98 (1993) 5648-5652.
[58] R. Ditchfield, W.J. Hehre, J.A. Pople, Self-Consistent Molecular-Orbital Methods. IX. An Extended Gaussian-Type Basis for Molecular-Orbital Studies of Organic Molecules, J. Chem. Phys., 54 (1971) 724-728.
[59] C.W. Bauschlicher, H. Partridge, A modification of the Gaussian-2 approach using density functional theory, J. Chem. Phys., 103 (1995) 1788-1791.
[60] J.P. Perdew, Density-functional Approximation for the Correlation Energy of the Inhomogeneous Electron Gas, Phys. Rev. B, 33 (1986) 8822-8824.
[61] Y. Zhao, D.G. Truhlar, The M06 Suite of Density Functionals for Main Group Thermochemistry, Thermochemical Kinetics, Noncovalent Interactions, Excited States, and Transition Elements: Two New Functionals and Systematic Testing of Four M06-Class Functionals and 12 Other Functionals, Theor. Chem. Acc., 120 (2008) 215-241.
[62] Y. Zhao, D.G. Truhlar, Density Functionals with Broad Applicability in Chemistry, Acc. Chem. Res., 41 (2008) 157.
[63] C. Möller, M.S. Plesset, Note on an Approximation Treatment for Many-Electron Systems, Phys. Rev., 46 (1934) 618-622.
[64] S.F. Boys, R. Bernardi, The Calculation of Small Molecular Interactions by the Differences of Separate Total Energies. Some Procedures with Reduced Errors, Mol. Phys., 19 (1970) 553-566.
[65] F.B. van Duijneveldt, J.G.C.M. van Duijneveldt-van de Rijdt, J.H. van Lenthe, State of the Art in Counterpoise Theory, Chem. Rev., 94 (1994) 1873-1885.
[66] J.T. O'Brien, E.R. Williams, Coordination numbers of hydrated divalent transition metal ions investigated with IRPD spectroscopy, J. Phys. Chem. A, 115 (2011) 14612-14619.
[67] S. Grimme, J. Antony, S. Ehrlich, H. Krieg, A Consistent and Accurate Ab Initio Parametrization of Density Functional Dispersion Correction (DFT-D) for the 94 Elements H-Pu, J. Chem. Phys., 132 (2010) 154104-154119.

[68] S. Grimme, S. Ehrlich, L. Goerigk, Effect of the Damping Function in Dispersion Corrected Density Functional Theory, J. Comput. Chem., 32 (2011) 1456-1465.
[69] T.E. Cooper, J.T. O'Brien, E.R. Williams, P.B. Armentrout, Zn^{2+} has a Primary Hydration Sphere of Five: IR Action Spectroscopy and Theoretical Studies of Hydrated Zn^{2+} Complexes, J. Phys. Chem. A, 114 (2010) 12646–12655.
[70] O.W. Wheeler, D.R. Carl, P.B. Armentrout, Second–Shell Thermochemistry for Hydration of Strontium Dications as Determined by Threshold Collision-Induced Dissociation and Computations, Int. J. Mass Spectrom., 429 (2018) 76-89.

Table 1. Theoretical Relative Enthalpies (ΔH_0) and Gibbs Energies (ΔG_{298})[a] (kJ/mol) for Hydrated Manganese Complexes [a]

	Complex (m,n,p)[b]	B3LYP		B3P86		M06		MP2(full)	
$Mn^{2+}(H_2O)_3$	(3,0)	**0.0**	**(0.0)**	**0.0**	**(0.0)**	**0.0**	**(0.0)**	**0.0**	**(0.0)**
	(2,1)	58.7	(58.4)	53.8	(53.5)	72.9	(72.6)	71.7	(71.4)
$Mn^{2+}(H_2O)_4$	(4.0)	**0.0**	**(0.0)**	**0.0**	**(0.0)**	**0.0**	**(0.0)**	**0.0**	**(0.0)**
	(3,1)_AA	53.4	(59.1)	51.4	(57.2)	67.7	(73.4)	57.7	(63.4)
	(3,1)_A	49.2	(45.0)	46.6	(42.5)	72.1	(67.9)	59.1	(55.0)
$Mn^{2+}(H_2O)_5$	(5,0)	**0.0**	**(0.0)**	**0.0**	**(0.0)**	**0.0**	**(0.0)**	**0.0**	**(0.0)**
	(4,1)_AA	8.9	(8.2)	7.8	(7.1)	27.1	(26.4)	18.5	(17.8)
	(4,1)_A	10.6	(6.9)	9.3	(5.6)	35.2	(31.6)	24.5	(20.8)
$Mn^{2+}(H_2O)_6$	(6,0)	**0.0**	(4,1)	**0.0**	(5.5)	**0.0**	**(0.0)**	**0.0**	**(0.0)**
	(5,1)_A_bA_b	2.9	**(0.0)**	1.5	**(0.0)**	26.2	(19.3)	15.0	(8.0)
	(5,1)_A_a	10.1	(1.4)	8.9	(1.7)	38.7	(26.0)	25.5	(12.8)
	(4,2)_4D_2AA	9.3	(13.0)	6.7	(11.8)	50.2	(49.9)	30.9	(30.6)
$Mn^{2+}(H_2O)_7$	(6,1)_AA	7.7	(4.2)	8.9	(5.4)	**0.0**	**(0.0)**	**0.0**	**(0.0)**
	(5,2)_4D_2A_bA_b	**0.0**	**(0.0)**	**0.0**	**(0.0)**	13.5	(17.0)	4.3	(7.8)
	(4,3)_4D_2A,AA	16.2	(3.2)	15.0	(2.0)	58.7	(49.2)	37.6	(28.1)
$Mn^{2+}(H_2O)_8$	(6,2)_4D_2AA_g	6.1	(4.3)	7.1	(5.3)	**0.0**	**(0.0)**	**0.0**	**(0.0)**
	(6,2)_4D_2AA_t	11.1	(6.0)	11.9	(6.8)	5.8	(2.5)	5.1	(1.8)
	(5,3)_4D,DD_2A_bA_b,A_bA_a	**0.0**	**(0.0)**	**0.0**	**(0.0)**	14.3	(16.1)	6.5	(8.3)
	(4,4)_2D,2DD_2A,2AA	16.2	(6.4)	15.6	(5.8)	58.1	(50.1)	38.4	(30.4)
$Mn^{2+}(H_2O)_9$	(6,3)_6D_3AA	**0.0**	(1.4)	**0.0**	(0.9)	**0.0**	**(0.0)**	**0.0**	**(0.0)**
	(5,4)_4DD_4A_bA_b	0.5	**(0.0)**	1.0	**(0.0)**	19.5	(17.5)	12.8	(10.9)
	(4,5)_D,3DD_3A,2AA	18.2	(4.7)	17.3	(3.3)	70.0	(55.0)	48.7	(33.8)

[a]ΔG_{298} values are given in parentheses. Values are single-point energies calculated at the level shown using a 6-311+G(2d,2p) basis set from geometries optimized at the B3LYP/6-311+G(d,p) level. Zero-point energy corrections are included. [b]See text for definitions of the nomenclature.

Table 2. Theoretical Relative Gibbs Energies (ΔG) at 215 and 305 K (kJ/mol) for $Mn^{2+}(H_2O)_6$ and Their Boltzmann Distributions[a]

Temperature	Complex (*m*,*n*,*p*)	B3LYP		B3LYP-GD3BJ[b]		B3P86		M06		MP2(full)	
215 K	(6,0)	2.8	15.4%	**0.0**	71.0%	4.2	7.8%	**0.0**	100.0%	**0.0**	99.4%
	(5,1)_A_bA_b	**0.0**	73.3%	1.7	28.0%	**0.0**	81.1%	20.6	0.0%	9.3	0.6%
	(5,1)_A_a	3.3	11.3%	7.6	1.0%	3.6	11.1%	29.2	0.0%	16.0	0.0%
305 K	(6,0)	4.2	10.7%	**0.0**	44.8%	5.6	6.7%	**0.0**	99.9%	**0.0**	95.1%
	(5,1)_A_bA_b	**0.0**	55.5%	**0.0**	44.3%	**0.0**	59.9%	19.2	0.1%	7.9	4.2%
	(5,1)_A_a	1.3	33.8%	3.6	10.9%	1.5	33.4%	25.7	0.0%	12.5	0.7%

[a]Except as noted, values are single-point energies calculated at the level shown using a 6-311+G(2d,2p) basis set from geometries optimized at the B3LYP/6-311+G(d,p) level. Thermal corrections at 215 and 305 K included. [b]Geometries were optimized at the B3LYP-GD3BJ/6-311+G(d,p) level and values are single-point energies calculated using a 6-311+G(2d,2p) basis set. Thermal corrections at 215 and 305 K are included.

Table 3. Optimized Parameters from Analysis of Cross Sections for Collision-Induced Dissociation of $Mn^{2+}(H_2O)_x$ Using Eqs. (4) and (4 × 6) [a]

x	Reactant	Product	σ_0	n	E_0 (PSL) (eV)	E_0 (No RRKM) (eV)	$\Delta S^{\dagger}_{1000}$ (J/mol K)
4	(4,0)	(3,0)[b]	70 (7)	0.4 (0.2)	1.77 (0.06)	2.04 (0.15)	29 (5)
		TS[2+1][c]	1 (1)		1.48 (0.08)		32 (1)
		(2,0)[d]	130 (50)		3.90 (0.06)		23 (5)
		TS[1+1][d]	22 (1)		3.24 (0.04)		17 (1)
5	(5,0)	(4,0)[b]	68 (3)	0.8 (0.1)	1.12 (0.07)	1.28 (0.15)	48 (5)
		TS[2+2][c]	85 (44)		1.40 (0.07)		81 (12)
		(3,0)[d]			2.87 (0.14)		23 (5)
		TS[2+1][d]			2.70 (0.15)		32 (1)
6	(5,1)	(5,0)[b]	80 (5)	1.1 (0.1)	0.89 (0.05)	0.97 (0.07)	77 (4)
	(6,0)	(5,0)[b]	79 (7)	1.1 (0.2)	0.91 (0.05)	1.00 (0.08)	68 (5)
		(4,0)[e]	77 (13)		2.17 (0.05)		58 (5)
7	(5,2)	(5,1)[b]	107 (7)	0.8 (0.1)	0.78 (0.04)	0.87 (0.05)	65 (4)
	(5,2)	(6,0)[b]	106 (6)	0.8 (0.1)	0.74 (0.04)	0.87 (0.05)	57 (4)
	(6,1)	(6,0)[b]	107 (7)	0.8 (0.1)	0.74 (0.04)	0.91 (0.05)	27 (4)
		(5,0)[e]	108 (8)		1.84 (0.03)		60 (5)
8	(5,3)	(5,2)[b]	95 (11)	1.0 (0.1)	0.73 (0.04)	0.84 (0.07)	55 (4)
	(6,2)	(6,1)[b]	97 (11)	1.0 (0.1)	0.74 (0.04)	0.86 (0.07)	71 (4)
		(6,0)[e]	91 (11)		1.58 (0.06)		20 (5)
9	(5,4)	(5,3)[b]	92 (4)	0.9 (0.1)	0.69 (0.03)	0.83 (0.04)	46 (4)
	(6,3)	(6,2)[b]	93 (5)	0.9 (0.1)	0.70 (0.04)	0.84 (0.05)	66 (4)
		(6,1)[e]	93 (5)		1.57 (0.05)		68 (5)

[a]Uncertainties (one standard deviation) in parentheses. Parameters listed are those for modeling with lifetime effects (PSL) considered. [b]Single channel modeling of total cross section using Eq. (4). [c]Competitive modeling of primary water loss and charge separation cross sections using Eq. (4). [d]Competitive sequential modeling of primary water and charge separation losses and secondary water loss cross sections using Eqs. (4) and (4 × 6). [e]Sequential modeling of primary product and secondary cross sections using Eqs. (4 × 6).

Table 4. Conversion of 0 K BDEs to 298 K Enthalpies and Gibbs Energies (kJ/mol) for $Mn^{2+}(H_2O)_x$[a]

x	Reactant	Product	ΔH_0[b]	ΔH_{298}-ΔH_0[c]	ΔH_{298}	$T\Delta S_{298}$[c]	ΔG_{298}
3	(3,0)	(2,0)	204.7 (3.4)	-8.1 (0.9)	196.6 (3.5)	-18.7 (2.6)	215.3 (4.4)
		TS[1+1]	140.2 (4.1)	-6.9 (0.6)	133.3 (4.1)	-45.7 (1.4)	179.0 (4.4)
4	(4,0)	(3,0)	170.9 (5.9)	1.6 (0.5)	172.5 (5.9)	34.6 (1.3)	137.9 (6.1)
		TS[2+1]	142.9 (7.7)	3.3 (0.2)	146.2 (7.7)	11.9 (0.1)	134.3 (7.7)
5	(5,0)	(4,0)	107.8 (7.0)	3.1 (0.6)	110.9 (7.0)	39.5 (1.3)	71.4 (7.1)
		TS[2+2]	135.4 (7.1)	6.5 (1.3)	141.9 (7.2)	27.5 (2.9)	114.4 (7.8)
6	(6,0)	(5,0)	87.4 (4.9)	1.7 (0.5)	89.1 (4.9)	45.7 (1.4)	43.4 (5.1)
7	(6,1)	(6,0)	71.6 (4.0)	2.9 (0.4)	74.5 (4.0)	32.3 (1.1)	42.2 (4.2)
8	(6,2)	(6,1)	71.8 (4.1)	4.3 (0.4)	76.1 (4.1)	45.9 (1.0)	30.2 (4.2)
9	(6,3)	(6,2)	67.7 (3.6)	4.2 (0.5)	71.9 (3.6)	44.3 (1.0)	27.6 (3.8)

[a]Uncertainties (one standard deviation) in parentheses. [b]Values are primary thresholds from Table 3 except for $x = 3$ which is a secondary value. [c]Values were calculated from the vibrational frequencies and rotational constants calculated at the B3LYP/6-311+G(d,p) level of theory. Uncertainties were found by scaling the vibrational frequencies up and down by 10%.

Table 5. Comparison of Experimental and Theoretical 0 K Hydration Energies (kJ/mol) for $Mn^{2+}(H_2O)_x$

x	Reactant	Product	Primary[a]	Secondary[a]	B3LYP[b]	B3P86[b]	M06[b]	MP2(full)[b]
1	(1,0)	Mn^{2+}			336.5 (338.6)	338.4 (340.5)	322.5 (324.8)	306.3 (313.5)
2	(2,0)	(1,0)			285.0 (287.8)	288.4 (291.3)	275.5 (278.7)	268.2 (277.0)
3	(3,0)	(2,0)		204.7 ± 3.4	205.5 (208.3)	208.3 (211.1)	215.3 (218.1)	201.0 (209.8)
4	(4,0)	(3,0)	170.9 ± 5.9	164.5 ± 2.2	162.6 (165.3)	165.1 (167.9)	183.4 (186.3)	162.9 (171.8)
5	(5,0)	(4,0)	107.8 ± 7.0	121.7 ± 3.4	105.1 (108.1)	107.7 (110.8)	129.7 (133.1)	111.7 (121.7)
6	(6,0)	(5,0)	87.8 ± 4.9	105.5 ± 2.5	92.8 (96.1)	94.8 (98.2)	121.7 (125.4)	101.7 (112.6)
	(5,1)	(5,0)	85.9 ± 4.9		90.1 (93.2)	93.6 (96.6)	96.3 (99.2)	88.7 (97.6)
7	(6,1)	(6,0)	71.6 ± 4.0	80.6 ± 3.9	74.0 (77.0)	77.0 (80.1)	78.5 (81.3)	73.2 (82.0)
8	(6,2)	(6,1)	71.8 ± 4.1	83.6 ± 4.3	74.9 (77.8)	77.6 (80.6)	80.3 (83.0)	74.7 (83.2)
9	(6,3)	(6,2)	67.7 ± 3.6		73.0 (75.9)	75.4 (78.4)	79.1 (81.8)	72.8 (81.1)
MAD[c]			4.9[d]	11.8	4.5 (5.7)	5.3 (7.4)	15.8 (18.9)	5.9[e] (12.5)
MAD[f]				3.3[d]	7.9 (6.1)	6.4 (5.3)	9.9 (11.3)	5.9 (3.6)

[a]Values from Table 3. [b]Theoretical values with (and without) cp correction. Single point energies calculated at the indicated level of theory using 6-311+G(2d,2p) basis set and B3LYP/6-311+G(d,p) geometries and zero-point energy corrections. [c]Mean absolute deviations from primary experimental BDEs using (6,0) value. [d]Mean experimental uncertainty. [e]Value drops to 4.0 if the primary BDE for $x = 6$ is assigned to (5,1). [f]Mean absolute deviations from secondary experimental BDEs using (6,0) value.

Table 6. Comparison of 0 K Transition State Energies and Hydration Enthalpies (kJ/mol)

x	Reactant	Product	Experiment	B3LYP[a]	B3P86[a]	M06[a]	MP2(full)[a]
3	(3,0)	(2,0)	205 ± 3[b]	205	208	215	201
		TS[1+1]	140 ± 4[c]	100	99	117	118
		$MnOH^+H_2O + H^+H_2O$		-85	-87	-67	-54
4	(4,0)	(3,0)	171 ± 6[b]	163	165	183	163
		TS[2+1]	143 ± 8[c]	140	139	160	162
		$MnOH^+(H_2O)_2 + H^+H_2O$		-24	-25	-3	6
5	(5,0)	(4,0)	108 ± 7[b]	105	108	130	112
		TS[(3,2)-(3,1,1)]		97	95	130	105
		TS[2+2]	135 ± 7[c]	92	89	138	125
		$MnOH^+(H_2O)_2 + H^+(H_2O)_2$		-63	-67	-17	-21

[a]Single point energies corrected for zero-point energy calculated at the indicated level of theory using 6-311+G(2d,2p) basis set with geometries and vibrational frequencies calculated at the B3LYP/6-311+G(d,p) level. [b]Values taken from Table 3 using the primary dissociation channel model for $x = 4 – 5$ and the sequential model for $x = 4$ to yield the $x = 3$ values listed here. [c]Values taken from Table 3 calculated by competitive analysis model, Eq. (4).

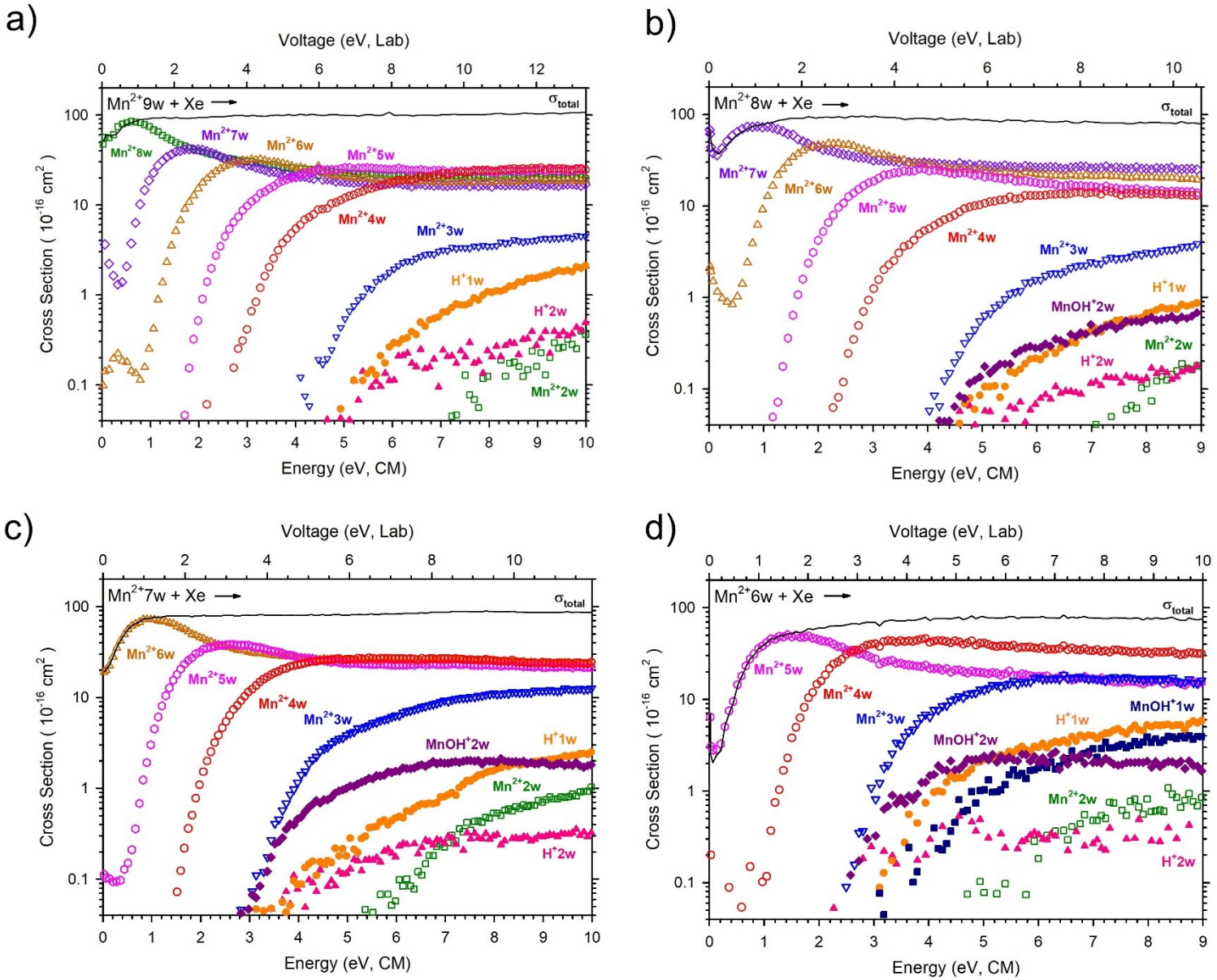

Figure 1. (continued)

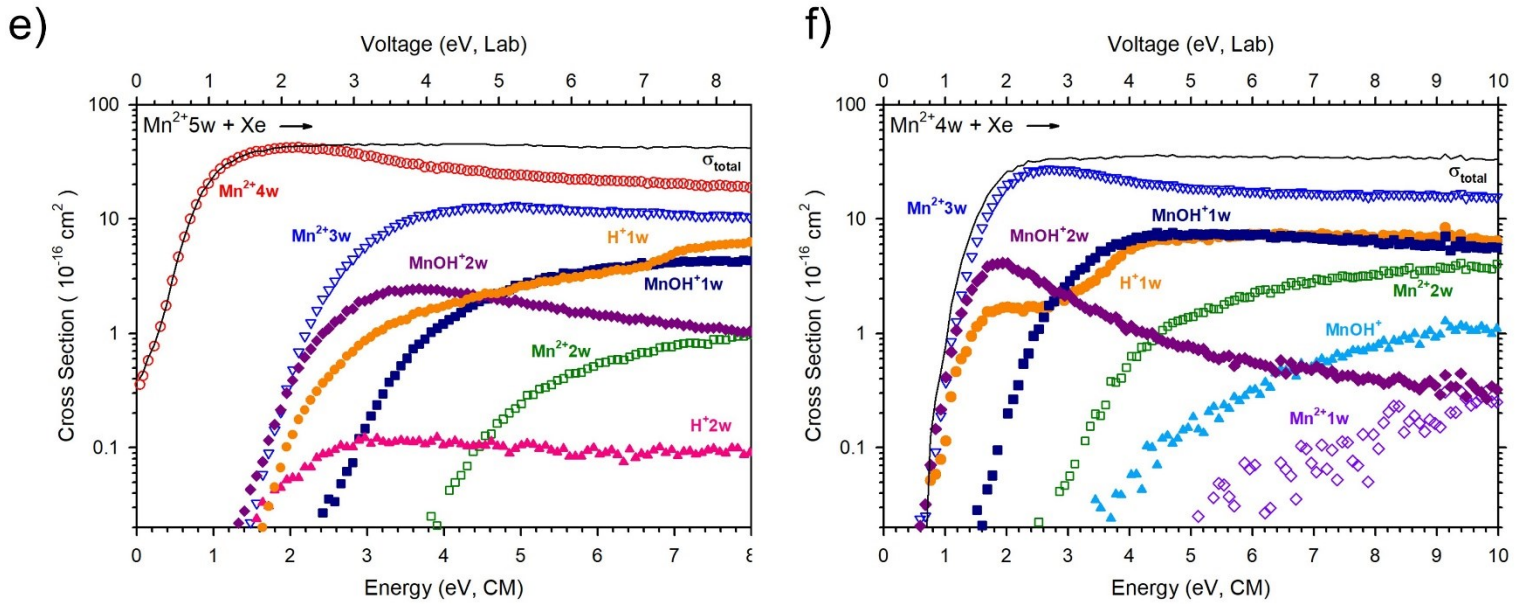

Figure 1. Cross sections for collision-induced dissociation of $Mn^{2+}(H_2O)_x$ where x = 4 – 9 (parts a – f) with Xe (~ 0.2 mTorr) as a function of kinetic energy in the center-of-mass frame (bottom x-axis) and applied voltage in the laboratory frame (top x-axis). Water loss products are represented by open symbols and charge separation products by closed symbols. In the labels, w represents H_2O.

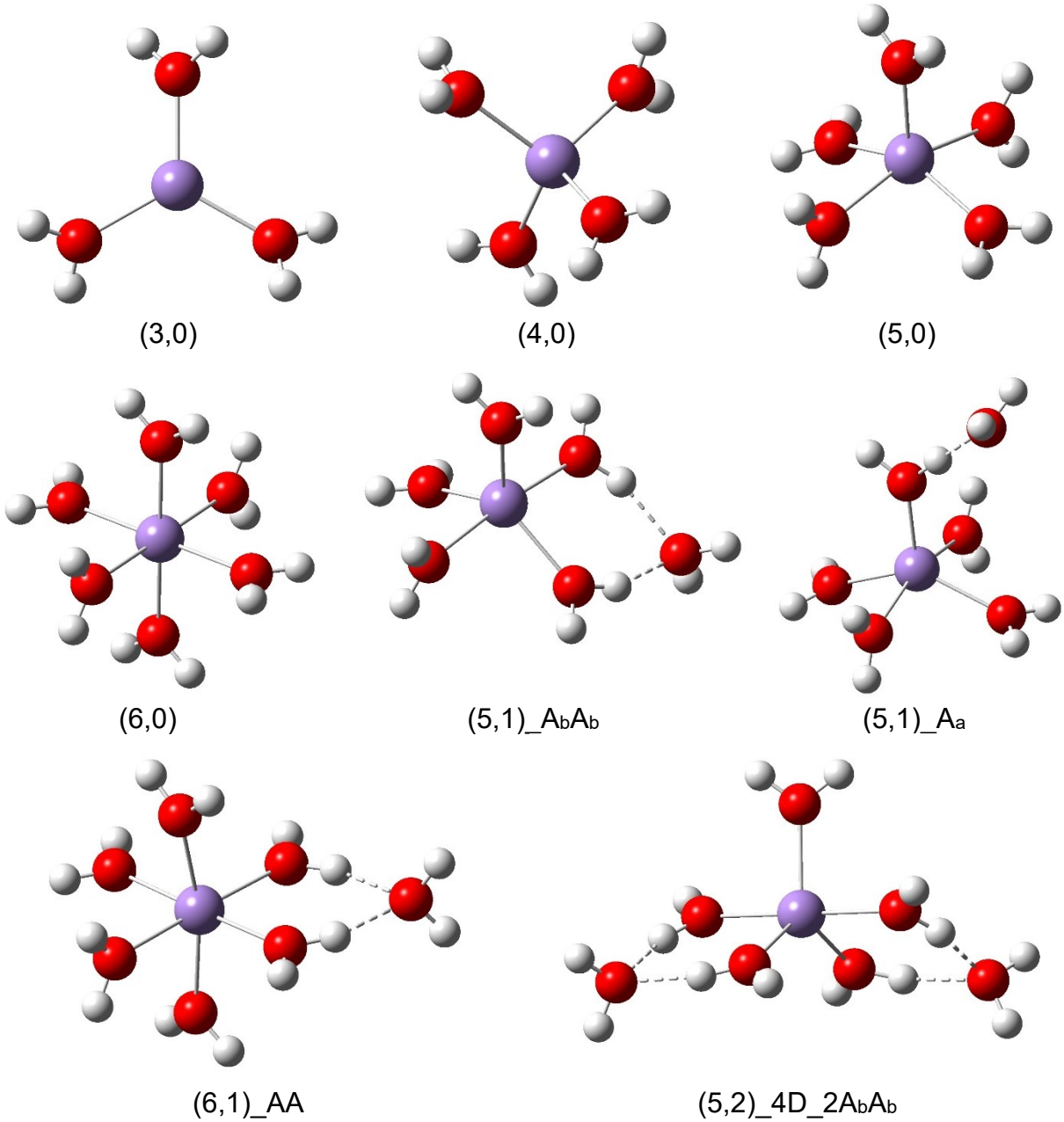

Figure 2. Geometries for the predicted ground structures of $Mn^{2+}(H_2O)_x$ complexes, $x = 3 – 9$, as optimized at the B3LYP/6-311+G(d,p) level of theory.

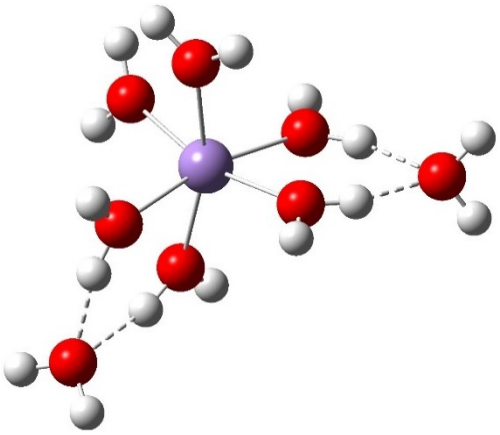

(6,2)_4D_2AAg

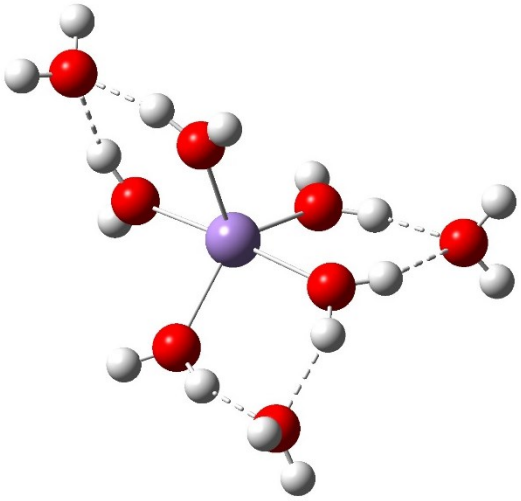

(5,3)_4D,DD_2A_bA_b,A_bA_a

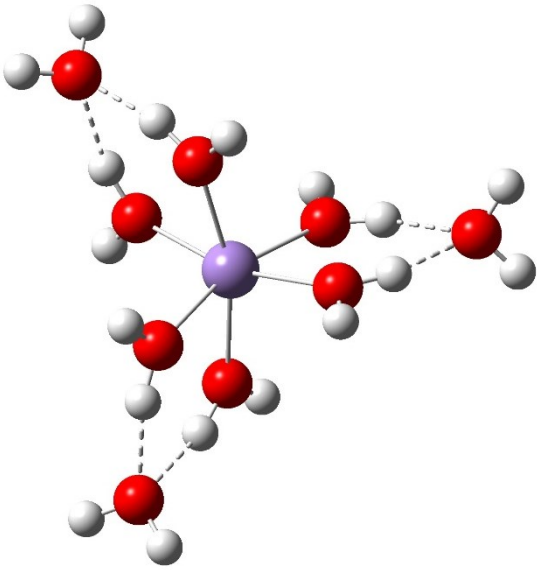

(6,3)_6D_3AA

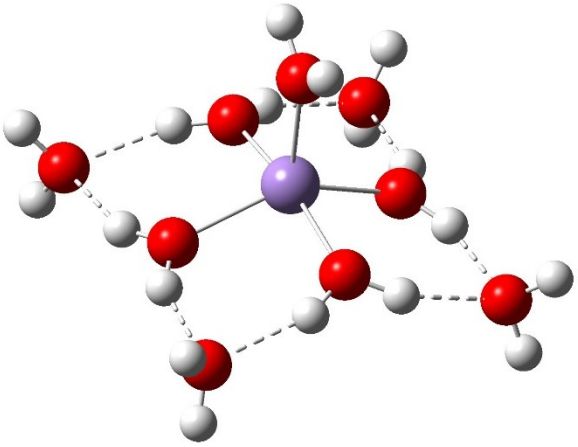

(5,4)_4DD_4A_bA_b

Figure 2. (continued)

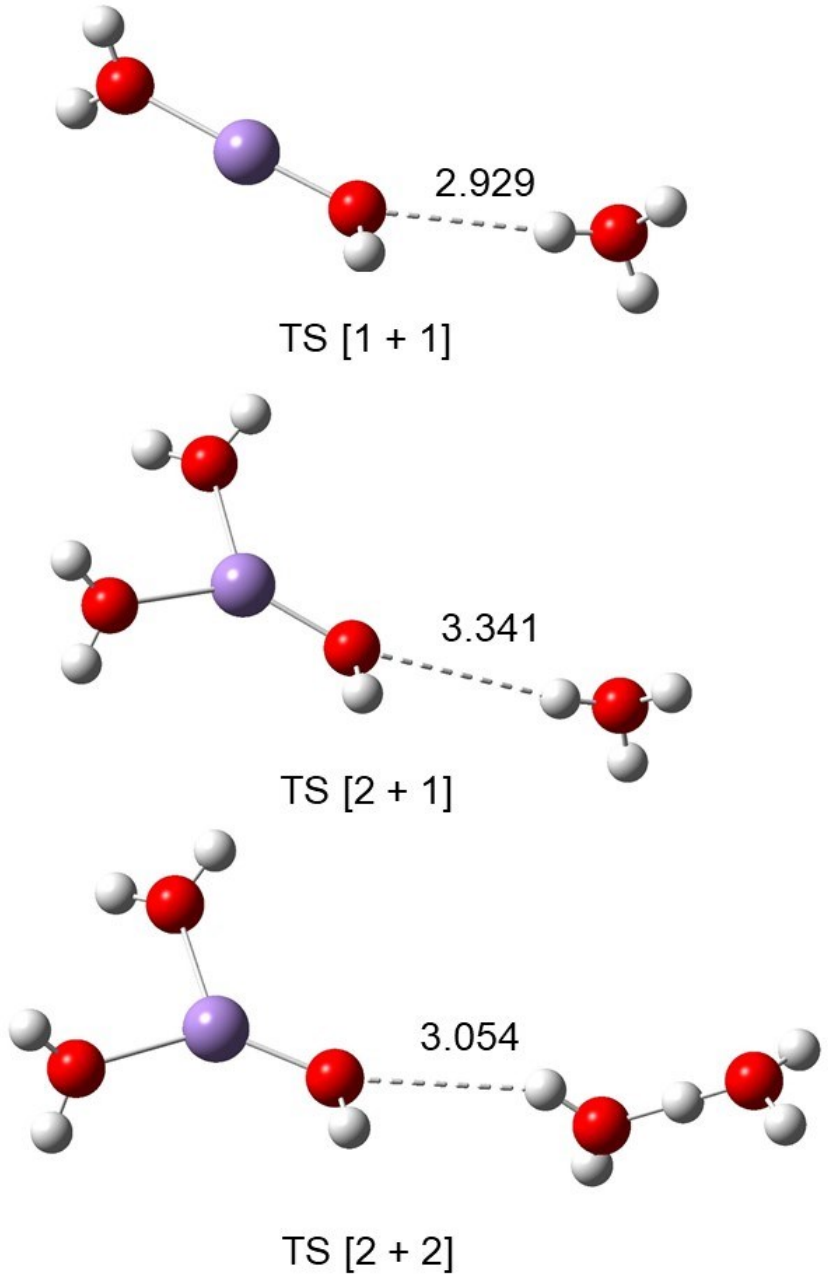

Figure 3. Possible rate-limiting charge separation transition states for reactions (7) – (9). Structures were optimized at the B3LYP/6-311+G(d,p) level of theory. TS[x + (x – y –1)] designates x, the number of water molecules directly bound to the $MnOH^+$ center, and (x – y – 1), indicates the number of water molecules bound to the leaving H^+. Bond lengths for the O-H bond being broken (dashed line) are provided in Å.

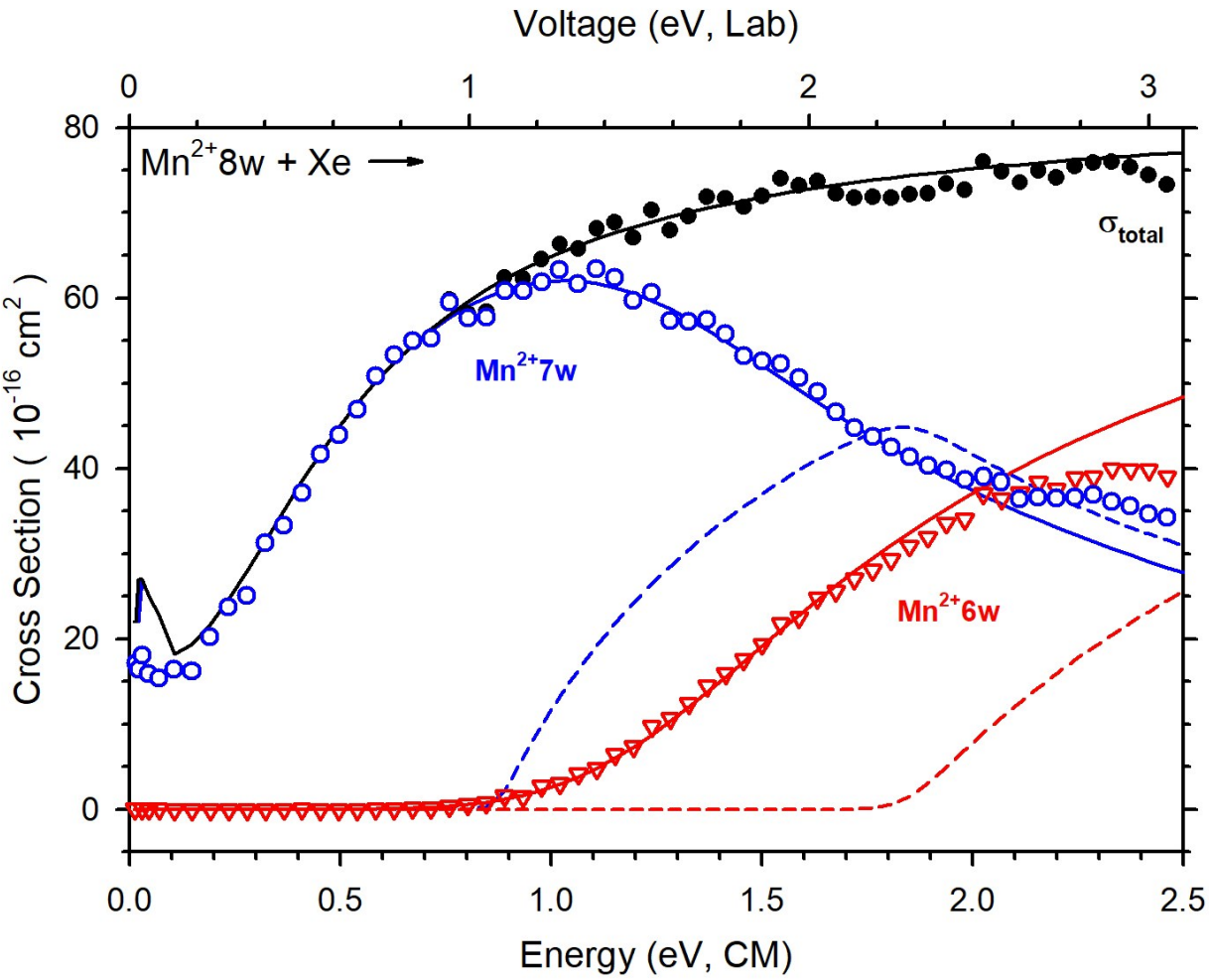

Figure 4. Zero-pressure extrapolated cross sections for the CID of $Mn^{2+}(H_2O)_8$ with higher order products not included. Solid lines show the best fits to the primary (open circles) and secondary (open triangles) water loss cross sections using Eq. (4 × 6) for the sequential model convoluted over the neutral and ion kinetic and internal energy distributions. Dashed lines show the models in the absence of experimental kinetic energy broadening for reactants with an internal energy of 0 K. Optimized parameters for these fits are found in Table 3. In the labels, w represents H_2O.

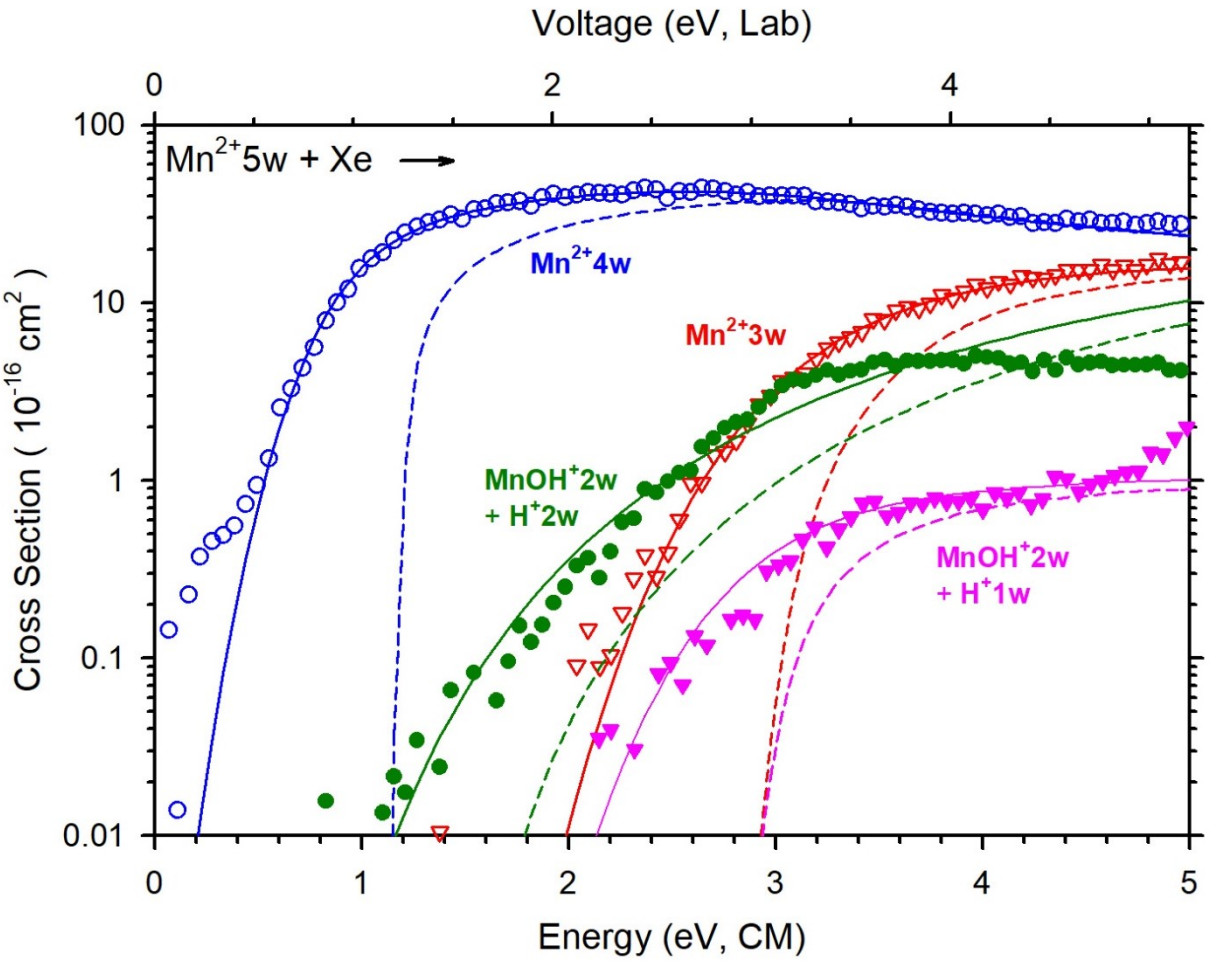

Figure 5. Zero-pressure extrapolated cross sections for the CID of $Mn^{2+}(H_2O)_5$. Solid lines show the best fits to the cross sections for primary water loss (open circles), the competing charge separation products (closed circles), secondary water loss (open triangles), and the competing charge separation products (closed triangles) using Eqs. (4) and (4 × 6) for the competitive sequential model convoluted over the neutral and ion kinetic and internal energy distributions. The dashed lines show the models in the absence of experimental kinetic energy broadening for reactants with an internal energy of 0 K. Optimized parameters for these fits are found in Table 3. In the labels, w represents H_2O.

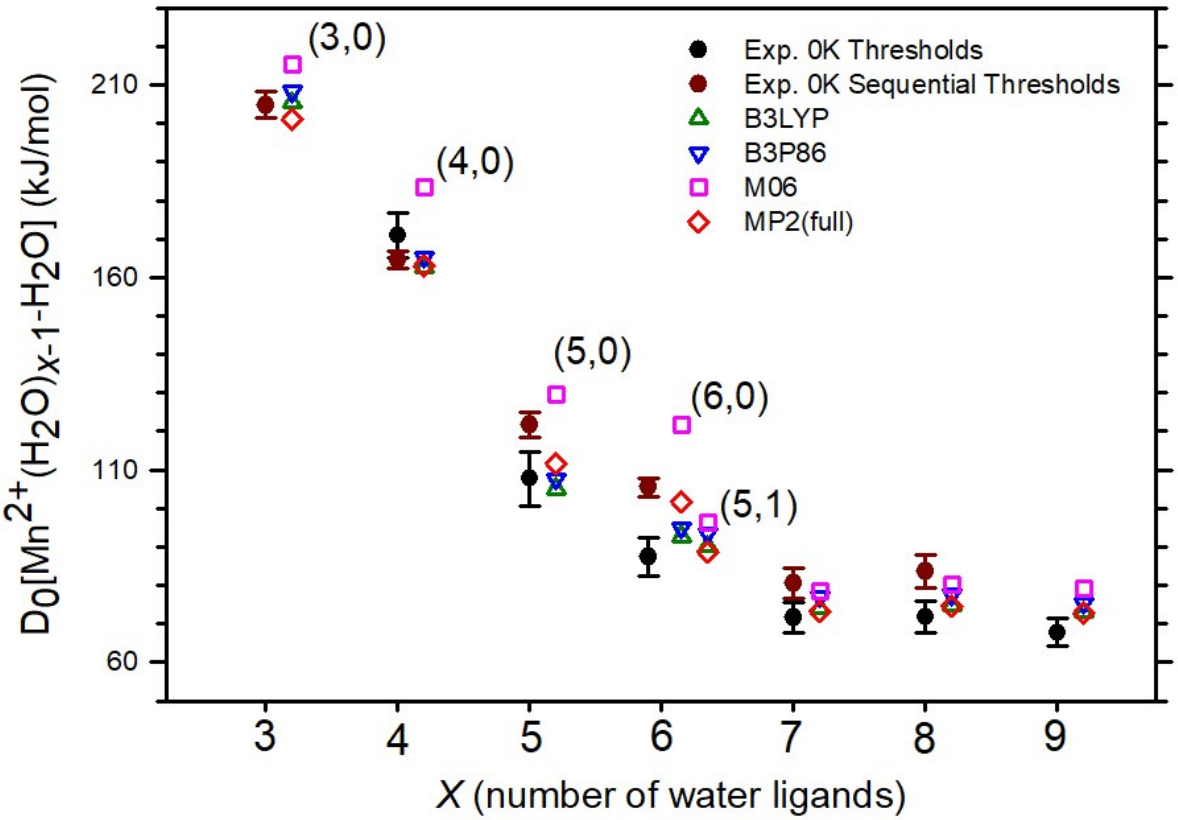

Figure 6. Comparison of experimental primary (black solid circles) and secondary (dark red solid circles) 0 K bond energies with theoretical B3LYP (open green up triangles), B3P86 (open blue down triangles), M06 (open pink squares) and MP2 values (open red diamonds), including cp corrections. Structures that are used for the theoretical BDE calculations are indicated in parentheses. For x = 7 – 9, B3LYP and B3P86 levels of theory predict (5, x-5) GSs, whereas M06 and MP2 predict (6, x-6) GSs.

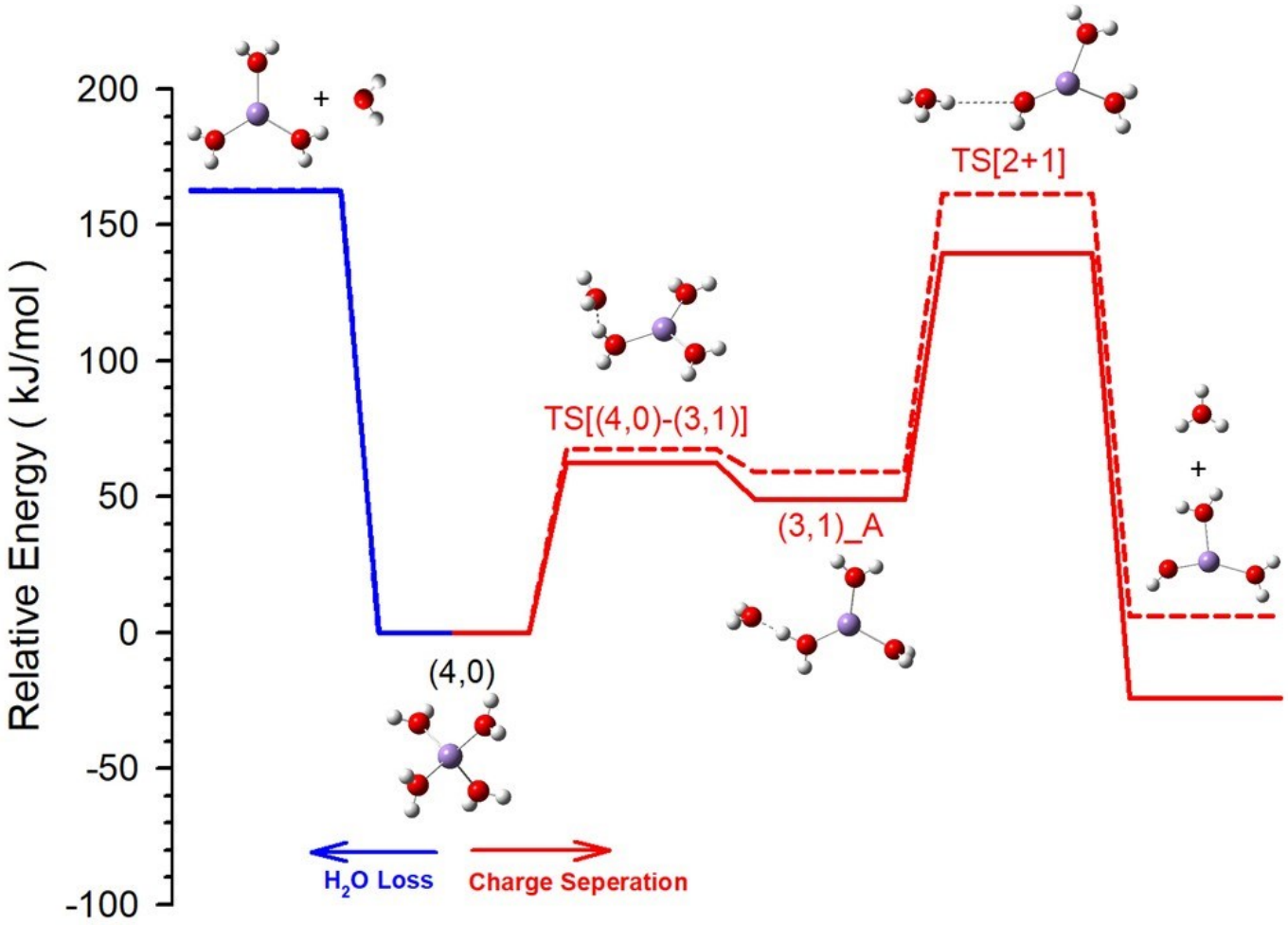

Figure 7. Reaction coordinates for water loss (blue) and charge separation (red) pathways of $Mn^{2+}(H_2O)_4$ from the (4,0) GS. Single point energies were calculated at the B3LYP (solid line) and MP2 (dashed line) levels of theory with the 6-311+G(2d,2p) basis set and include zero-point energies.

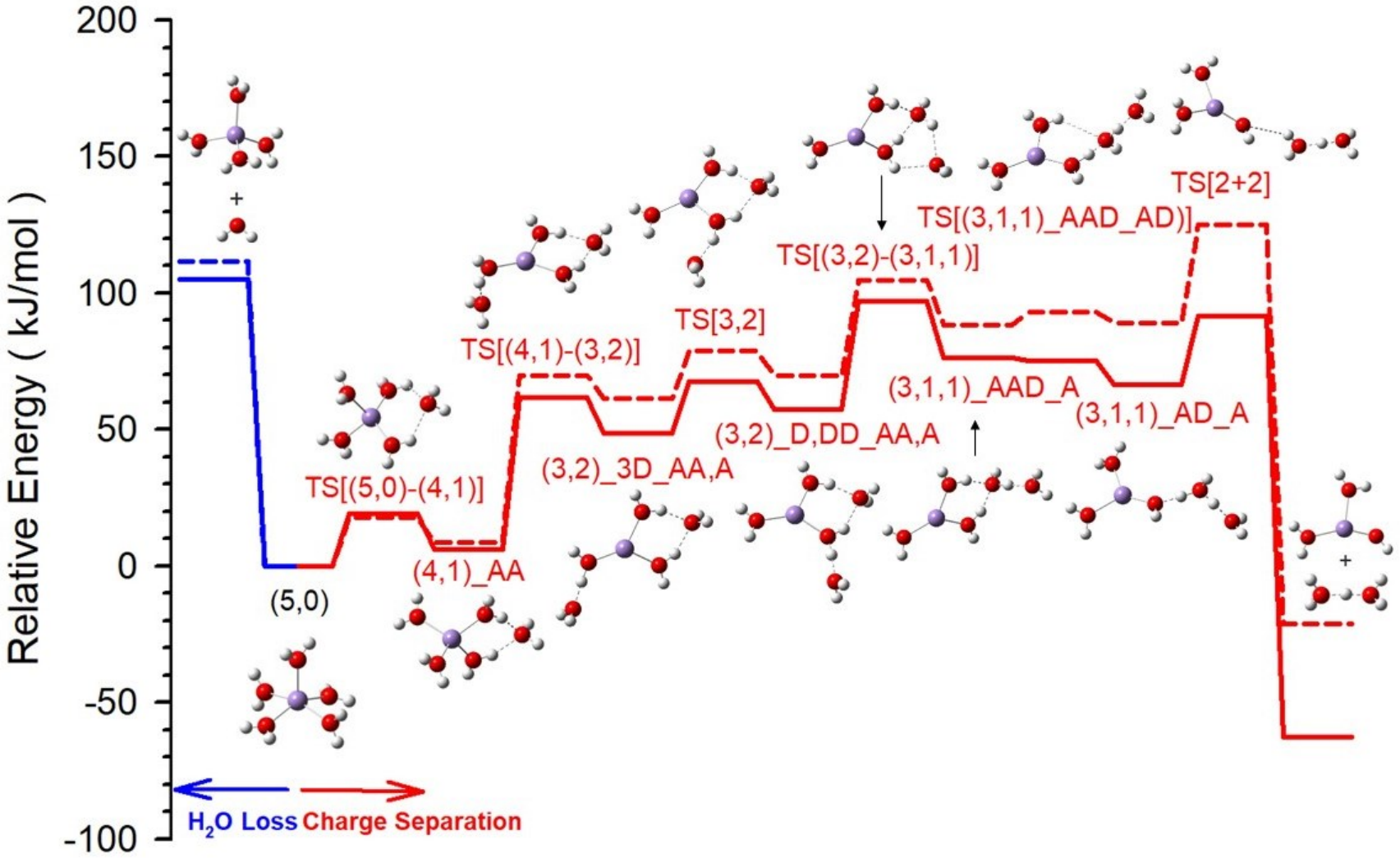

Figure 8. Reaction coordinates for water loss (blue) and charge separation (red) pathways of $Mn^{2+}(H_2O)_5$ from the (5,0) GS. Single point energies were calculated at the B3LYP (solid line) and MP2 (dashed line) levels of theory with the 6-311+G(2d,2p) basis set and include zero-point energies.